RESEARCH ARTICLE

HELiPOD — Revolution and evolution of a helicopter-borne measurement system for multidisciplinary research in demanding environments

Falk Pätzold[1,*], Lutz Bretschneider[1], Stefan Nowak[1,2], Björn Brandt[3], Andreas Schlerf[1], Magnus Ole Asmussen[1], Sven Bollmann[1], Konrad Bärfuss[1], Barbara Harm-Altstädter[1], Peter Hecker[1], Birgit Wehner[4], Berend G. van der Wall[5], Torsten Sachs[6], Heidi Huntrieser[7], Anke Roiger[7], and Astrid Lampert[1]

The helicopter-borne measurement system HELiPOD is a platform for atmospheric and other environmental measurements to investigate local and regional phenomena. It can be operated in remote areas, as from a research vessel with a helicopter, without the need for a runway. This article presents the current design concept, technical details, and sensor package of HELiPOD, which was completely renewed for the deployment during the MOSAiC (Multidisciplinary drifting Observatory for the Study of Arctic Climate) expedition across the North Polar Ocean in 2019/2020. It was updated for the deployment in the methane campaigns METHANE-To-Go-Poland to study methane emissions from coal mines in South Poland, and METHANE-To-Go-Nordstream, a follow-up campaign to study methane emissions from the Baltic Sea after the NordStream pipeline leaks in 2022. The HELiPOD has the dimensions of 5.2 m × 2.1 m × 1.2 m and a weight of around 325 kg. It provides the possibility for flight patterns on a horizontal scale of typically 100 m–100 km and at altitudes from 10 m up to 3 km. HELiPOD employs distributed data acquisition and central data synchronization, equipped with sensors relevant to five fields of research: atmospheric dynamics, trace gases, aerosols, radiation, and surface properties. The focus of this article is the technical realization, in particular the data acquisition system for about 60 sensors, as well as concepts for energy supply and thermal management. It describes the complementary use of different measurement principles and redundant sensors for improved data quality. Operational procedures are also discussed.

1. Introduction
The helicopter-borne probe HELiPOD (see **Figure 1**) was developed in the early 1990s with the goal of sampling the atmosphere at very low altitudes and with high spatial resolution in order to study interaction processes between surface and atmosphere. Originally, HELiPOD was equipped with sensors for measuring the basic meteorological parameters at high temporal resolution: wind vector, air temperature, and humidity (Bange and Roth, 1999). It has been used for investigating the impact of small-scale surface heterogeneity on sensible and latent heat fluxes (Bange et al., 2002). During several expeditions to the Arctic Ocean, HELiPOD was deployed from the research vessel *Polarstern* (Knust, 2017) in 1994, 1995, and 2003 (e.g., Fahrbach, 1995; Krause, 1996; Muschinski and Wode, 1998; Schauer and Kattner, 2004; van den Kroonenberg and Bange, 2007). In 2008, it was used to investigate the changes of the wind field and in particular turbulence behind wind turbines (Emeis et al., 2016). Further, HELiPOD was operated in the Lena Delta, Siberia, in 2012 and 2014 to study the spatial variability of methane emissions from a permafrost landscape (Lampert et al., 2018).

[1] Institute of Flight Guidance, Technische Universität Braunschweig (TU Braunschweig), Braunschweig, Germany

[2] Leichtwerk AG, Braunschweig, Germany

[3] messWERK GmbH, Braunschweig, Germany

[4] Department of Experimental Aerosol and Cloud Microphysics, Leibniz Institute for Tropospheric Research (TROPOS), Leipzig, Germany

[5] Institute of Flight Systems, German Aerospace Center (DLR), Braunschweig, Germany

[6] German Research Centre for Geosciences, Telegrafenberg, Potsdam, Germany

[7] Institute of Atmospheric Physics, German Aerospace Center (DLR), Oberpfaffenhofen-Wessling, Germany

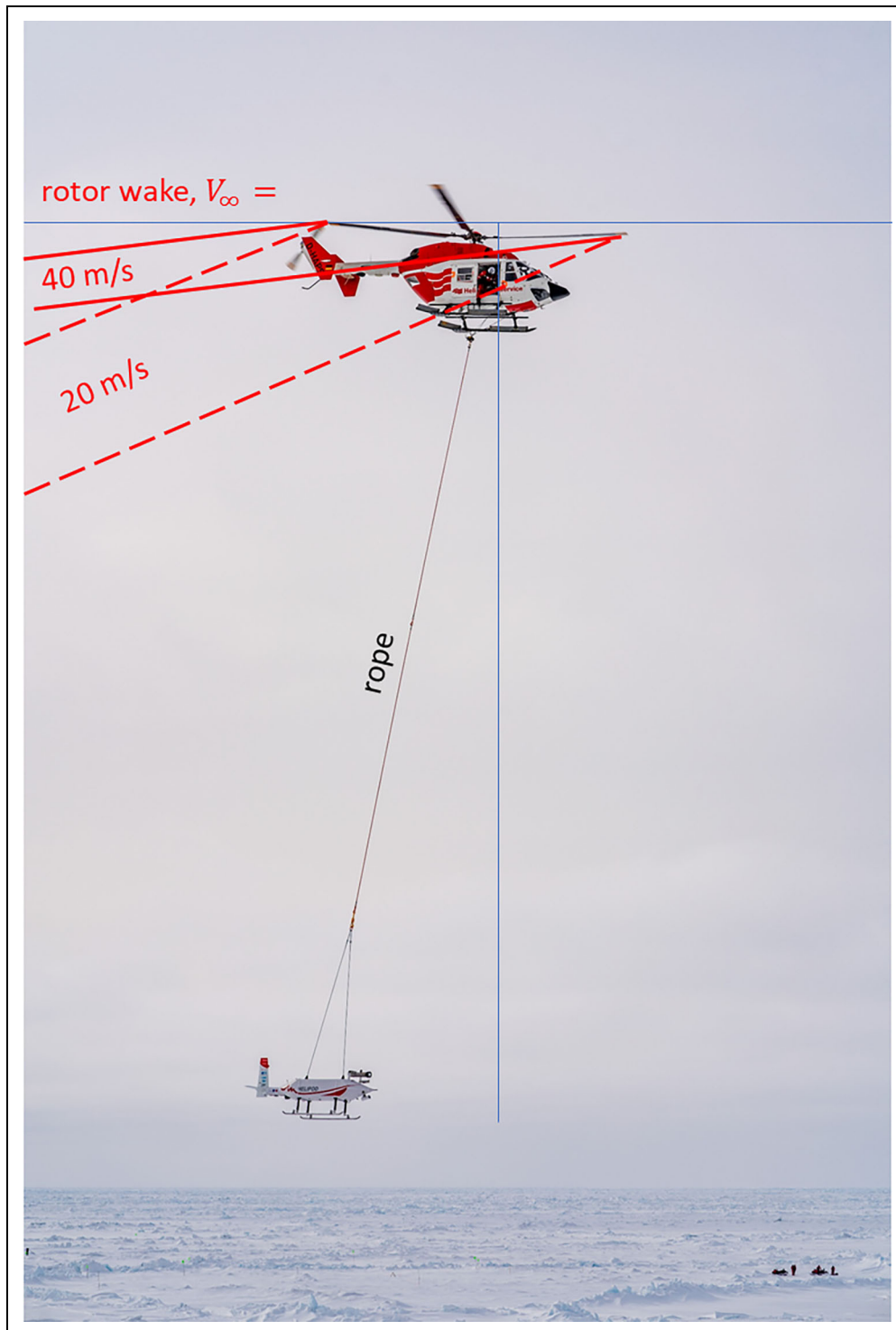*Corresponding author:
Email: f.paetzold@tu-braunschweig.de

Figure 1. HELiPOD after takeoff during MOSAiC with illustration of the rotor downwash area for the measurement speed of 40 m s^{-1} and for an airspeed of 20 m s^{-1}. Picture: C. Rohleder.

Based on the experience with the initial system and in particular its meanwhile outdated data acquisition, it was decided to modernize HELiPOD completely for further applications. Since then, it has been developed into a multidisciplinary environmental observation probe.

For atmospheric research, airborne systems provide a much higher flexibility, accuracy, and spatial resolution than ground-based or satellite-based observation systems (Martin et al., 2011) and can be equipped with different instruments depending on the scope of the measurements. A large variety of airborne platforms are currently available for different applications, covering the range from unmanned systems for sampling on the scale of several kilometers (e.g., Lampert et al., 2016; Lampert et al., 2020a; Lonardi et al., 2022) to research aircraft with different endurance, flight altitudes, and payload capacities (Drüe and Heinemann, 2007; Lampert et al., 2020b). For instance, the research aircraft HALO (High-Altitude

Long-Range), based on the business jet G550, was utilized in multiple campaigns by the German Aerospace Center (DLR), for example, from 2013 to 2016 for investigating cloud properties and their environmental conditions over the North Atlantic (Konow et al., 2019). To study atmospheric boundary layer processes, as well as the regional and local greenhouse gas emissions, typically smaller research aircraft are used, such as the Cessna Grand Caravan of the German Aerospace Center DLR (e.g., Fiehn et al., 2020; Klausner et al., 2020; Kostinek et al., 2021).

In this context, a special case is helicopter-based atmospheric measurement systems. They fill particular operational gaps, where they have advantages over other systems: In remote areas that are accessible by vessels with a helicopter on board, they can be operated flexibly without requiring additional infrastructure like a prepared runway. Compared to drones, they can carry a noticeably larger payload and have a much larger range of operation, which is typically limited to visual line of sight for drones or requires a sophisticated safety concept and redundancy. Further, some countries have strict regulations that do not allow the deployment of foreign research aircraft. In combination with a nationally registered helicopter, atmospheric measurements can be enabled more easily. Sometimes, it is easier to get a permission to fly at low altitude with a helicopter than with a fixed-wing aircraft. Compared to research aircraft, helicopters can be operated at much lower air speed, which allows a higher spatial resolution of measurement data for a given measurement frequency, or even hover, which is done for picking up and setting down the HELiPOD. Due to the missing propulsion system, helicopter-towed sondes experience a much lower level of vibrations, which is an advantage for some sensors (Lampert et al., 2018). Another advantage is that the sensor system is legally treated as an external sling load, which the helicopter pilot can drop in case of an emergency, as no electric connection to the helicopter is necessary. Therefore, the complex aviation certification process for operating sensors on an aircraft is not necessary.

However, a possible disadvantage is the rotor downwash during takeoff and landing. In cruise flight, the significant forward speed and the length of the rope bring the towed system far outside the helicopter rotor disturbance, as the downwash angle is at medium single-digit degrees.

Only a few helicopter-borne meteorological sensor systems are in operation today: Besides HELiPOD, the ACTOS (Airborne Cloud Turbulence Observation System) is operated by the Leibniz Institute for Tropospheric Research (TROPOS) for investigating clouds and aerosol particles (Siebert et al., 2006; Siebert et al., 2013). The concept is to fly the helicopter above the cloud top and operate the ACTOS system with a rope of 200 m length directly in clouds, when no icing conditions are present (Wehner et al., 2015; Siebert et al., 2021).

This article presents the overall concept, technical details, and the sensor package of HELiPOD, as it was operated during the MOSAiC (Multidisciplinary drifting Observatory for the Study of Arctic Climate) expedition (Nicolaus et al., 2022; Rabe et al., 2022; Shupe et al., 2022) and updated for the METHANE-To-Go-Poland

project (in the following simply called "METHANE-To-Go") in 2022. Section 2 describes the design of the overall system to meet the requirements imposed by the 60 sensors of different research fields of the atmosphere and for providing a link to other disciplines, like sea ice and biogeochemistry. Section 3 introduces the technical basis of the redesigned system: This includes the data acquisition and the data management system designed for the specific sensor configuration in Section 3.1. The thermal system is introduced in Section 3.2, the power system is presented in Section 3.3, and the data postprocessing is described in Section 3.4. Section 4 briefly describes the operational experiences and gives an overview of the HELiPOD flights during the field experiments MOSAiC and METHANE-To-Go. Section 5 provides a summary and conclusion. We do not present measurement data from field campaigns, which is left for pending scientific analyses and manuscripts in preparation.

2. HELiPOD design concept and instrumentation

In this section, the starting point of HELiPOD is provided: At the beginning of the modernization, it was decided to use the HELiPOD structural and mechanical system as reliably applied in the past and to select an appropriate sensor package. Therefore, the HELiPOD concept is briefly introduced in Section 2.1, and an overview of the chosen instrumentation is provided in Section 2.2.

2.1. Design concept

The HELiPOD is basically a containment for sensors that can be attached to a helicopter as a so-called sling load. It consists of three sections, the nose section, which is most appropriate for undisturbed atmospheric measurements, the center section with the largest payload capacity, and the aft section. For transport, these sections can be separated. With a suitable length of the connecting rope of around 25 m, the HELiPOD is far outside of the helicopter's downwash.

To ensure atmospheric measurements of the HELiPOD free of turbulence caused by the helicopter rotor wake, an estimation of its orientation in space is performed here. It is based on momentum theory (Leishman, 2000), which provides information about the mean value of induced velocities normal to the rotor disk, v_i.

The origin of these is the rotor thrust T, the magnitude of v_i is depending on the rotor disk area $A = \pi R^2$ with R as rotor radius, its inclination with respect to the oncoming flow α, and the flight speed V_∞. The general solution is a quartic equation for v_i, which can only be solved numerically. The generally small angles α allow for a good estimate when assuming $\alpha = 0$, which enables an analytic solution. With $v_h = 1.1\sqrt{T/(2\rho A)}$ as the effective mean-induced velocity in the hovering case at zero flight speed $V_\infty = 0$ m s^{-1} and ρ as air density, the mean-induced velocity in forward flight and thus the inclination of the rotor wake slipstream relative to the horizon $\phi_{wake} = \arctan(v_i/V_\infty)$ can be computed by:

$$v_i = \sqrt{\sqrt{V_\infty^4/4 + v_h^4} - V_\infty^2/2}. \tag{1}$$

We compute a wake inclination angle of $\phi_{\mathrm{wake}} = 6.5^{\circ}$ for an assumed rotor thrust, T, equal to the helicopter and payload weight (BK117 C1 maximum takeoff mass including the attached HELiPOD assumed as 3.5 t and the rotor radius of 5.5 m) and a flight speed of 40 m s^{-1}, which are the approximate measurement parameters. Therefore, the wake is just striking the top of the helicopter's fuselage but is far from the rope and the attached HELiPOD, as illustrated in **Figure 1**. Visualizations of the wake geometry during real flights are shown in Bauknecht et al. (2017). Due to the drag of the HELiPOD, the rope shows an angle of ca. 78°, relative to the horizon. By this simple analysis, the minimum flight speed can also be estimated that allows measurements without affecting the HELiPOD, depending on the overall mass, height (via air density ρ), and the helicopter characteristics (via A and T).

To provide favorable airflow conditions at the 5-hole probe and air inlets, the instrument containment is aerodynamically stabilized, using a conventional passive empennage at the rear end. The overall weight of HELiPOD is currently 325 kg, with 105 kg of scientific payload during MOSAiC in 2020, and 135 kg during METHANE-To-Go in 2022. The total length is 5.2 m, the height of the vertical fin is 2.1 m, and the width at the skids is 1.2 m. The outer size of the square shaped center section is 0.65 m × 0.65 m.

The need for stabilizing the inside temperature follows from the demands of the chosen instrumentation, see further description of the thermal system provided in Section 3.2.

The power supply can be realized via different approaches: electrical power from the helicopter, which requires a sufficient excess of power in the helicopter electrical system, a proof that there is no interaction with the helicopter's electrical system and a certified quick release plug in case of emergency releasing the external load. The alternative is a battery-powered energy storage integrated into the HELiPOD, reducing its scientific payload capacity, but allowing for complete independence from the helicopter in use (see Section 3.3).

During the planning of the transpolar drifting experiment MOSAiC, the participation of HELiPOD was considered for various reasons: HELiPOD provides the unique opportunity of investigating atmospheric conditions on a horizontal scale of several 10 km, thus significantly exceeding the range of the central observatory and distributed observatories, which were established close to *Polarstern* (Shupe et al., 2022). This makes it possible to estimate the representativeness of the measurements performed at the central observatory and the spatial variability of different parameters. Compared to aircraft observations, HELiPOD is operated near the ship, thus covering mainly the direct vicinity of the investigation area. Further, HELiPOD can be equipped with a multitude of sensors in addition to the classical meteorological sensors and constitutes a link for coupling atmosphere, sea ice, radiation, and biogeochemistry by simultaneous observations.

Finally, HELiPOD provides the flexibility to perform flight paths as required for different purposes. For example, this can be vertical profiles for investigating the atmospheric stability. Another typical flight pattern consists of flight legs at very low altitudes of around 10 m, depending on the environmental conditions and the helicopter operations, to study the interaction of surface and atmosphere, for example, by the calculation of momentum, heat, and trace gas fluxes (see **Figure 2**, left). A suitable flight pattern to investigate the distribution of pollutants from a point source can be upwind and downwind legs aligned perpendicular to the main wind direction at various distances and altitudes (see **Figure 2**, right).

In the following, an overview of the applied sensors and the challenges of integrating them into the HELiPOD system are presented.

2.2. Sensor overview

Figure 3 illustrates the numerous sensors installed in HELiPOD during the MOSAiC campaign. The instruments were selected to cover five different fields of research in a balanced and complementary way:

- atmospheric boundary layer dynamics (Section 2.2.1),
- aerosol properties (Section 2.2.2),
- trace gases (Section 2.2.3),
- radiation budget (Section 2.2.4), and
- surface properties (Section 2.2.5).

Additionally, different camera systems like a 360° camera were included to record visual impressions of the missions. The sensors for each research field were selected according to the relevance for the respective mission, the complementarity to other sensors, the availability at the Institute of Flight Guidance of TU Braunschweig and cooperating partners, and the ease of integration into the HELiPOD concerning weight, dimensions, and power consumption.

In addition, the sensors had to be integrated into the HELiPOD taking into account different limitations. The overall weight constraints for the entire system had to be respected. The weight is limited by the static design of the probe and the limitations of each component, as well as the maximum takeoff weight that the helicopter can carry as external sling load. Furthermore, all sensors require power supply, and a power supply system was newly developed for the particular needs of the sensors and the mission (see Section 3.3). Most of the sensors are temperature dependent and require a stable temperature within certain limits, setting the requirements for the thermal system (see Section 3.2).

Subsequently, the sensors deployed on HELiPOD are briefly introduced. Technical details of the sensors contributing to each field of research are provided in **Tables 1–7**.

2.2.1. Atmospheric boundary layer dynamics
To fully characterize atmospheric boundary layer dynamics, the measurements of the meteorological parameters, such as temperature, humidity, and wind vector are essential. The approach of the system is to combine sensors with
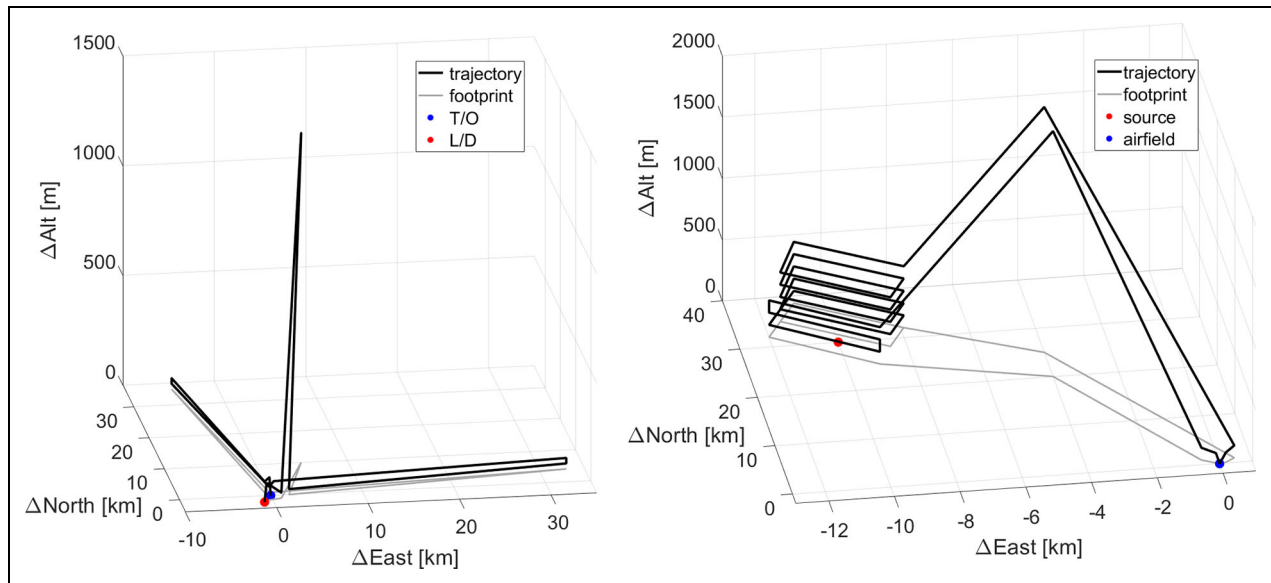
Figure 2. Exemplary schematic flight paths. Left: Outbound and return legs parallel and rectangular to the main wind direction at 50 m above ground at outbound and 25 m at return leg with a vertical profile up to 1,500 m at the end. T/O (takeoff) and L/D (landing) are at the same place. Right: Investigation of a point source (red) with upwind and downwind legs rectangular to the main wind direction at different altitudes and vertical profiles up to 2,000 m on the way to the region of interest and on the way back to the airfield (blue).
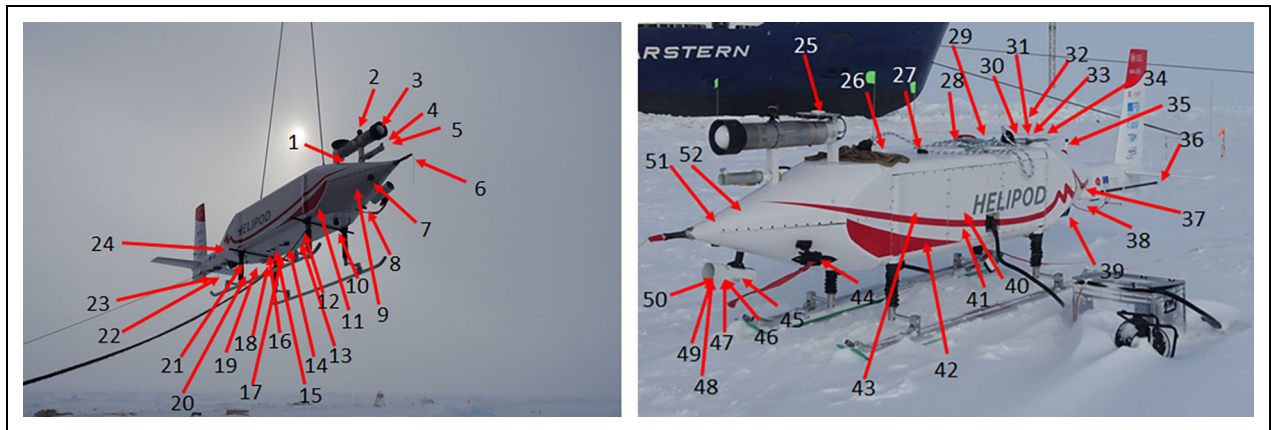
Figure 3. HELiPOD during MOSAiC. Left: HELiPOD is lifted by a vessel crane onto the floe before a measurement flight. The red arrows indicate the locations of the various sensors that are installed on board and introduced in the text. Right: HELiPOD in front of *Polarstern* on sea ice. Pictures: F. Pätzold. The numbers indicate the location of the following sensors, inlets, and antennas: (1) aerosol sensor inlet, (2) camera Kodak Pixpro, (3) LICOR7700, (4) radiation sensor ML01, (5) LICOR7500A, (6) 5-hole probe, (7) Rosemount 102BW, (8) closed path humidity sensor inlet, (9) ozone sensor air inlet, (10) camera Kodak Pixpro, (11) IMU Litef, (12) KT19, (13) MLX90614, (14) camera EOS, (15) camera Photon Focus, (16) camera FLIR A65, (17) camera Gobi640, (18) CMP22, (19) MLX90614, (20) ML01, (21) CRG4, (22) radar altimeter ERT180, (23) radar altimeter UUMR, (24) ML01, (25) front GNSS antenna Novatel 7720 for iNAT200, (26) GNSS antenna Javad Delta, (27) camera EOS, (28) upward directed WiFi antenna, (29) GNSS antenna Javad Delta, (30) CRG4, (31) MLX90614, (32) ML01, (33) CMP22, (34) rear GNSS antenna Novatel 7720 for iNAT200, (35) horizontally focusing WiFi antenna, (36) ML01, (37) ML01, (38) 3-axis magnetometer, (39) VLP16, (40) aircore, (41) 12 bags air sampler, (42) 12 bags air sampler, (43) aircore, (44) open path Lyman-Alpha L6, (45) open path housing, (46) 4× fine wire temperature sensor, (47) 2x Pt1000, (48) TSYS01, (49) HMP110, (50) Rapid P14, (51) 4x Setra pressure sensors (connected to 5-hole probe), and (52) 4x AMS5812 pressure sensors (connected to 5-hole probe). More information on the sensors can be found in **Tables 1–6**. GNSS = global navigation satellite system.

different characteristics, like highly accurate sensors with low response time, with sensors of high response time, but lower absolute accuracy (see Section 3.4.3). For redundancy and quality control, several sensors of the same type and sensors based on different measurement principles were deployed upon availability. Furthermore, sensors were integrated in different ways, either directly exposed to the free flow (the so called open path

Table 1. Overview of HELiPOD meteorological sensors with information on the measured parameter, the company/manufacturer, the sensor name, the measurement principle, additional comments, accuracy according to data sheet, if not stated differently, and the number to identify the sensor position in Figure 3

Parameter	Company	Sensor	Method, Resolution	Comments	Accuracy	No.
Static pressure	Setra	270	Absolute pressure, 100 Hz	5-hole probe	±0.03% FS[a]	51
Dynamic pressure	Setra	239	Differential pressure, 100 Hz	5-hole probe	±0.14% FS[a]	51
Angle of attack	Setra	239	Differential pressure, 100 Hz	5-hole probe	±0.14% FS[a]	51
Angle of sideslip	Setra	239	Differential pressure, 100 Hz	5-hole probe	±0.14% FS[a]	51
Static pressure	AMSYS	5812-0150-B	Absolute pressure, 100 Hz	5-hole probe	<1.0% FS[a]	52
Dynamic pressure	AMSYS	5812-0001-D-B	Differential pressure, 100 Hz	5-hole probe	<1.0% FS[a]	52
Angle of attack	AMSYS	5812-0001-D-B	Differential pressure, 100 Hz	5-hole probe	<0% FS[a]	52
Angle of sideslip	AMSYS	5812-0001-D-B	Differential pressure, 100 Hz	5-hole probe	<1.0% FS[a]	52
Temperature	Rosemount	102BW	Pt100 resistive, 100 Hz	Open path	±0.3 K	7
Temperature	IFF	Fine wire set 1	2×Pt fine wire res.,[b] 100 Hz	Open path	±0.1 K	46
Temperature	IFF	Fine wire set 2	2×Pt fine wire res.,[b] 100 Hz	Open path	±0.1 K	46
Temperature	TSYS	TSYS01	Resistive, 100 Hz	Open path	±0.1 K	48
Temperature	Vaisala	HMP110	Pt1000 resistive, 1.7 Hz	Open path	±0.4 K	49
Temperature	LICOR	LI7500A and LI7700	Resistive, 20 and 40 Hz	Open path	n/a[c]	3, 5
Temperature	Vaisala	HMP110	Pt1000 resistive, 1.7 Hz	Closed path	±0.4 K	
Humidity	Vaisala	HMP110	Capacitive, 1.7 Hz	Open path	±1.5%	49
Humidity	IST[d]	P14	Capacitive, 1.5 Hz	Open path	±1.5%	50
Humidity	Buck	Lyman-Alpha	Optical-UV,[e] 100 Hz	Open path	n/a[c]	44
Humidity	LICOR	LI7500A	Optical-IR,[f] 20 Hz	Open path	2% of ppt[g]	5
Humidity	Buck	Lyman-Alpha	Optical-UV,[e] 100 Hz	Closed path	n/a[c]	8
Humidity	Vaisala	HMP110	Capacitive, 1.7 Hz	Closed path	±1.5%	8
Humidity	Meteolabor	TP3-ST	Dew point mirror, 2 Hz[h]	Closed path	±0.25 K (DP[i])	8
Humidity	Meteolabor	Snow White	Dew point mirror, 2 Hz[h]	Closed path	±0.2 K (DP[i])	8
Humidity	GE[j]	1011B	Dew point mirror, 1°C s^{-1}	Closed path	±0.1 K (DP[i])	8

[a]Full scale.

[b]Resistive.

[c]Not available.

[d]Innovative Sensor Technology.

[e]Ultraviolet.

[f]Infrared.

[g]Parts-per-trillion, 10^{-12}.

[h]Strongly depending on temperature.

[i]Dew point.

[j]General eastern.

configuration) or in a closed-path cell with controlled flow rate. An overview of the meteorological sensor package is provided in **Table 1**.

The high-resolution fine-wire resistance temperature sensor was developed at the Institute of Flight Guidance (Bärfuss et al., 2018). A comparison of airborne applications of the two different optical humidity sensors, the Lyman-Alpha (Buck, 1976), and the infrared absorption sensor LI7500 (LICOR, USA), is shown in Lampert et al. (2018).

The flow through the closed path Lyman-Alpha was measured with a flow sensor (SFM3000, Sensirion,

Table 2. Overview of HELiPOD position and attitude sensors with information on the measured parameter, the company/manufacturer, the sensor name, the temporal resolution, additional comments, and the number to identify the sensor position in Figure 3

Parameter	Company	Sensor	Resolution (Hz)	Comments	Accuracy	No.
Position	Javad	Delta-3	1	2 systems onboard	±1.5 cm (RTK,[a] pp[b])	26, 29
Position	ublox	ZED-F9P	10	METHANE-To-Go	±1 cm (RTK,[a] pp[b])	
Position	iMAR	iNAT-M200/SLN	500	Dual antenna	±3 cm (RTK,[a] pp[b])	25, 34
Attitude	iMAR	iNAT-M200/SLN	500	MEMS-IMU	<0.5°/h	25, 34
Attitude	Analog Devices	ADIS16488	98.4	METHANE-To-Go	<5.1°/h	
Attitude	LITEF	LLN-G1	64	FOG-IMU	≤0.05° (static)	11
Magnetic field	Magson	EnExMag	100	3-axis magnetometer (2×)	<2 arcsec	38
Radar height	Thomson-CSF	ERT 180	100	Radar altimeter	±2 ft	22
Radar height	smartmicro	UURM-0A	100	Radar altimeter	Max 0.5 m or 3%	23

[a]Real-time kinematic.

[b]Postprocessing.

Table 3. Overview of HELiPOD aerosol sensors with information on the measured parameter, the company/manufacturer, the sensor name, the size of aerosol or wavelength of optical instrument, additional comments, and the accuracy according to the manufacturer

Parameter	Company	Sensor	Size, Wavelength (nm)	Resolution (Hz)	Comments	Accuracy	No.
Number concentration	TSI	3007	>5	1	Via thermodenuder	±20%	nn
Number concentration	TSI	3007	>11	1	Via thermodenuder	±20%	nn
Number concentration	MetOne	GT-526S	>300	1	Via thermodenuder	±15%	nn
Number concentration	TSI	3007	>5	1	No thermodenuder	±20%	nn
Number concentration	TSI	3007	>10	1	No thermodenuder	±20%	nn
Number concentration	MetOne	GT-526S	>300	1	No thermodenuder	±15%	nn
Absorption coefficient	Brechtel	9406	450, 525, 624	1	Direct inlet	±0.2 M m^{-1}	nn

The aerosol sensors are all located inside the HELiPOD in the nose section, thus are not numbered (nn) in **Figure 3**. However, they have a joint inlet, indicated by number 1 in **Figure 3**.

Switzerland), and the flow rate through the dew point mirrors was regulated with a flow controller (MCRW-10SLPM-D-DM9M, Alicat Scientific, USA).

The wind vector is calculated based on the difference between the HELiPOD ground speed vector and the airspeed vector (Axford, 1968). The ground speed vector is determined from a combination of global navigation satellite system (GNSS) data available at 10-Hz resolution and the higher resolution data of the inertial measurement unit. The airspeed vector of the HELiPOD, in contrast, is determined from pressure measurements, where the total pressure, static pressure, and differential pressures on a multihole probe are measured to determine the true airspeed and the flow angles, the angle of attack, and angle of sideslip.

For calculating the three-dimensional wind vector at 100 Hz, different sensors are involved: A multihole probe (Rosemount, USA) was used with pressure sensors to determine the flow field and combined with high resolution attitude data. The differential pressure between total and static pressure (the dynamic pressure) is required for calculating the true airspeed, and the differential pressure between the up- and downward-oriented hole as well as between the left- and right-hand-orientated hole is used for determining the angle of attack, respectively, the angle of sideslip. The technology of determining the wind vector and methods of calibration are equal to the state-of-the-art research aircraft; thus, the uncertainty of the wind measurement is comparable (see, e.g., Lampert et al., 2020a).

Several navigation sensors (inertial measurement units, GNSS/GNSS receivers) were integrated to determine the HELiPOD position and attitude. Two 3-axis magnetometers were installed. The height above the surface was measured with 2 radar altimeters.

Table 4. Overview of HELiPOD trace gas sensors with information on the measured parameter, the company/manufacturer, the sensor name, the measurement principle and temporal resolution, additional comments, and the number to identify the sensor position in Figure 3

Parameter	Company	Sensor	Principle, Resolution	Comments	Accuracy	No.
CO_2 mole fraction	LICOR	LI7500A	IR[a] absorption, 20 Hz	Open path	0.16 ppm[b]	5
CH_4 mole fraction	LICOR	LI7700	IR[a] absorption, 40 Hz	Open path	5 ppb[c]	3
O_3 mole fraction	2B Technol.	M205	UV[d] absorption, 0.5 Hz	Closed path	>1.0 ppb[c]	9
Air sampling		Multifoil bags	Extractive	Laboratory analyses	Not available	41, 42
Air sampling		AirCore	Extractive	Laboratory analyses	Not available	40, 43

[a]Infrared.

[b]Parts-per-million, 10^{-6}.

[c]Ultraviolet.

[d]Parts-per-billion, 10^{-9}.

Table 5. Overview of HELiPOD radiation sensors with information on the measured parameter, the company/manufacturer, the sensor name, the wavelength range, additional comments, and the number to identify the sensor position in Figure 3

Parameter	Company	Sensor	Wavelength	Resolution/ Response Time	Comments	Accuracy	No.
Upward solar irradiance	Kipp&Zonen	CMP22	210–3,600 nm	<1.7 s	Pyranometer	5 W m^{-2}	18
Downward solar irradiance	Kipp&Zonen	CMP22	210–3,600 nm	<1.7 s	Pyranometer	5 W m^{-2}	33
Upward solar irradiance	EKO	ML-01	400–1,100 nm	<1 ms	Pyranometer	±2%	20
Downward solar irradiance	EKO	ML-01	400–1,100 nm	<1 ms	Pyranometer	±2%	24
Backward solar irradiance	EKO	ML-01	400–1,100 nm	<1 ms	Pyranometer	±2%	32
Forward solar irradiance	EKO	ML-01	400–1,100 nm	<1 ms	Pyranometer	±2%	4
Left solar irradiance	EKO	ML-01	400–1,100 nm	<1 ms	Pyranometer	±2%	36
Right solar irradiance	EKO	ML-01	400–1,100 nm	<1 ms	Pyranometer	±2%	37
Upward terrestrial irradiance	Kipp&Zonen	CGR4	4.5–42 μm	<18 s	Pyrgeometer	4 W m^{-2}	21
Downward terrestrial irradiance	Kipp&Zonen	CGR4	4.5–42 μm	<18 s	Pyrgeometer	4 W m^{-2}	30

The sensors for determining position and attitude are given in **Table 2**.

2.2.2. Aerosol properties

For investigating the aerosol microphysical properties, different sensors were included. An overview of the aerosol sensor package is provided in **Table 3**.

To measure different size classes, two sets of aerosol instruments were deployed, each consisting of one optical particle counter (OPC, model GT-526S, Met One Instruments Inc., USA) and two modified condensation particle counters (CPC, model 3007, TSI Inc., USA) with different lower cutoff diameters operating at 1-Hz sampling rate.

The air flow of the first setup of aerosol sensors went through a thermodenuder heated to a temperature of 150°C to distinguish between volatile and nonvolatile aerosol constituents (e.g., Wehner et al., 2002). The aerosol sensors were calibrated at the Leibniz Institute of Tropospheric

Research (TROPOS), and the threshold diameters of the CPCs of the second setup (without thermodenuder) were determined as 5 and 11 nm, respectively. However, the CPC with the lower threshold diameter of the first setup (behind thermodenuder) could not be characterized properly during the calibration after the campaign; thus, the cutoff diameter was taken from the first calibration before MOSAiC, resulting in a particle size of 5 nm. The cutoff diameter of the second CPC from the first setup was determined as 11 nm. The difference between the particle number concentrations of both CPCs provides the particle number concentration in the size range 5–11 nm, an indicator of new particle formation (Altstädter et al., 2015; Platis et al., 2016).

Both OPCs measure aerosol particle number concentration via 6 different size channels between 300 nm and 10 μm, which allows to study accumulation and coarse mode particles. Additionally, a single channel tricolor absorption photometer (STAP 9406, Brechtel, USA) was

Table 6. Overview of HELiPOD surface sensors with information on the measured parameter, the company/manufacturer, the sensor name, the wavelength range and temporal resolution, additional comments, and the number to identify the sensor position in Figure 3

Parameter	Company	Sensor	Wavelength, Resolution	Comments	Accuracy	No.
Surface temperature	Heitronics	KT19	8–14 μm, 21 Hz	IR[a] radiometer	±0.5°C	12
Surface temperature	MELEXIS	MLX90614ESF	5.5–14 μm, 1 Hz	IR[a] radiometer	±0.5°C	13, 19, 31
Surface VIS images	PF[b]	MV1	VIS,[c] 1 Hz	VIS[c] cam.	10% resp.[d]	15
Surface IR images	FLIR	A65	IR,[a] 1 Hz	IR[b] cam.	±5% reading	16
Surface IR images	Gobi	640	IR,[a] 1 Hz	IR[a] cam.	±0.05°C	17
Surface VIS images	EOS	EOS-RP	VIS,[c] 1/3 Hz	Fish eye camera	n/a[e]	14
Sky VIS images	EOS	EOS-RP	VIS,[c] 1/3 Hz	Fish eye camera	n/a[e]	27
Upward semispheric video	PIXPRO	SP360 4K	1 Hz	360° camera	n/a[e]	2
Downward semispheric video	PIXPRO	SP360 4K	1 Hz	360° camera	n/a[e]	10
Surface roughness	Velodyne	VLP-16	300 kHz	Laser scanner	±3 cm	39

[a]Infrared.

[b]Photon focus.

[c]Visible.

[d]Peak responsivity.

[e]Not available.

Table 7. Additional sensors implemented for the METHANE-To-Go project.

Parameter	Company	Sensor	Method	Resolution/ Response Time	Accuracy
CH_4 mole fraction	Picarro	G2401-m	Optical	1 Hz	2 ppb[a]
CO_2 mole fraction	Picarro	G2401-m	Optical	1 Hz	200 ppb[a]
Water vapor mole fraction	Picarro	G2401-m	Optical	1 Hz	150 ppm[b]
Soot concentration	AethLabs	MA200	Optical attenuation	1 Hz	Not available
Particle number concentration	MetOne	GT526-S	Optical attenuation	1 Hz	±10%
CO	Alpha Sense	CO-B4	Electrochemical	1 Hz/<30 s	±4 ppb[a]
NO	Alpha Sense	NO-B4	Electrochemical	1 Hz/<45 s	±15 ppb[a]
NO_2	Alpha Sense	NO2-B43F	Electrochemical	1 Hz/<80 s	±15 ppb[a]
O_x ($NO_2 + O_3$)	Alpha Sense	Ox-B431	Electrochemical	1 Hz/<80 s	±15 ppb[a]
Fast humidity	Sparv Embedded	SKS21	Capacitive	10 Hz	<1.5% RH[c]
Fast temperature	Sparv Embedded	SKS21	Thermistor	10 Hz	<0.1 K
Ultrafast temperature	Not available	Fine wire	Resistive	20 kHz	Not available

[a]Parts-per-billion, 10^{-9}.

[b]Parts-per-million, 10^{-6}.

[c]Relative humidity.

included to determine the equivalent black carbon mass concentration (eBC) from the particle light absorption coefficient based on the method of three-wavelength optical attenuation for the wavelengths $\lambda_{blue} = 450$ nm, $\lambda_{green} = 525$ nm, and $\lambda_{red} = 624$ nm. The detection limit is given to ±0.2-Mm^{-1} or 20-ng m^{-3} eBC mass concentration, as specified by the manufacturer. More information about the aerosol measurement unit deployed on HELiPOD is available in Lampert et al. (2020a), which presents the same aerosol sensors, but deployed on the
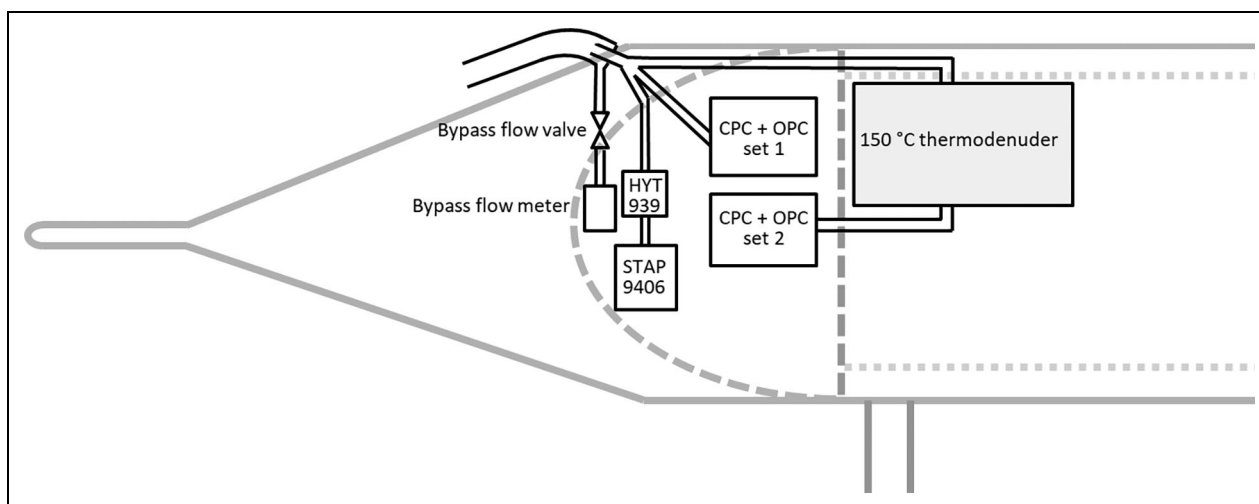
Figure 4. Tubing scheme of the aerosol sensors in HELiPOD. Two sets comprising each two condensation particle counters (CPC) and one optical particle counter (OPC) were included, one attached directly to the inlet and the other via a thermodenuder heated to 150°C. The black carbon sensor STAP (Single channel Tricolor Absorption Photometer) was attached to the inlet flow via a temperature and humidity sensor (HYP 939). The flow through the aerosol sensors was controlled by internal pumps and the bypass flow was controlled as well.

fixed-wing drone called ALADINA (Altstädter et al., 2015), which was used as a basis module for setting up the aerosol compartment shown here.

On HELiPOD, the aerosol instruments are placed in the nose section to realize short inlet lines. All instruments are connected to one stainless steel tubing as inlet. Laminar flow splitters are used to distribute the sample flow among the different instruments. Aerosol sampling requires laminar conditions in all sampling lines.

This can be ensured if the Reynolds number is below a critical value, which was set at 2,000 to be on the safe side. The Reynolds number depends on the inner diameter of the tube and the corresponding flow. If the flow becomes too high, it gets turbulent. The laminar flow splitters used in the aerosol sampling line have the purpose to divide one flow into two or more outlet flows. They collect the flow from the inner part of a flow to avoid wall artifacts and allow isokinetic sampling from inside a tube. This ensures to measure a representative aerosol sample. The flow splitter also minimizes particle losses. All further connections are also realized by conductive material. **Figure 4** illustrates the setup of the aerosol sensors in the HELiPOD. The inlet was placed on top of the nose section in undisturbed air. The sensors were all provided with air from the same inlet. One set of two CPCs and one OPC was connected directly to the inlet, with one pump and flow controller for the set. The second set of two CPCs and one OPC was fed by air heated up to 150°C through the thermodenuder, which was placed in the center part due to space restrictions, for removing the volatile aerosol fraction. The STAP was connected directly to the inlet via a temperature and humidity sensor for potentially correcting effects.

The flow through the sensors was controlled by internal pumps and flow meters, and the bypass flow in the order of 20% of the total flow was controlled and measured separately.

2.2.3. Trace gases

For investigating biogeochemical processes, and in particular for determining the Arctic Ocean and sea ice as sources or sinks of the greenhouse gases carbon dioxide (CO_2) and methane (CH_4), different sensors were integrated. An overview of the trace gas sensor package is provided in **Table 4**. An ozone (O_3) sensor was included, as the reactive species O_3 may have an impact on aerosol and precursor gases.

Two air sampling systems were included, each containing 12 sampling bags with an individual volume of 750 mL. After flights, the sampled air probes are analyzed in the laboratory, for example, concerning the CH_4 isotopic composition, similar to the procedures shown in Lampert et al. (2020c).

The bags are fitted in single mechanical chambers in a depressurized compartment. The pump (3KQ Boxer, UK) provides a pressure level of 90 hPa and can reestablish this pressure within roughly 30 s after one bag is filled, so the filling condition for each bag is equal.

The inner pressure of the depressurized compartment is measured. Each bag is fitted with a self-sealing quick connector produced by the company CPC and plugged to the counterpart on a magnet valve. The bags are emptied when installed in the system by applying a pump like it is used to depressurize the compartment. The valves can be opened manually for this step. Inflight the pump can be switched on and off by the operator in the helicopter, and the measured pressure is displayed to control the process. The magnet valves are triggered manually in the current setup. The filling process of one bag takes around 2.2 s, and the triggered valves are closed after 4 s. Two or more valves can be triggered at the same time, which results in slightly increased filling times, depending on the number of bags to be filled at the same time. A typical application of this feature is a double sampling for controlling the

chain of methods (see Lampert et al., 2020c). After a valve was triggered in flight, it is locked for the rest of the flight to avoid accidental reopening. All states and actions are recorded in the data acquisition.

As the air sampling system is operated remotely, it is not possible to use manual valves. In addition, the material of the bags is stressed by the filling process, so the idea was to use multilayer material like Linde multifoil. No commercial bag distributor was able to deliver customized bags with the right size and the chosen connector, and it was not possible to weld multilayer foils; therefore, medical infusion bags were chosen, which were rated as extra diffusion tight. However, it turned out in the field that the air sampled in the bag contained a significant number of small size particles. Thus, finding the right material is ongoing work. In addition, two AirCore systems with a length of 49.1 m, an outer diameter of 3.175 mm, and a wall thickness of 0.127 mm, resulting in a volume of 358 mL, were integrated, which store air in a small capillary (Andersen et al., 2018; Vinković et al., 2022). They can be analyzed after the flight and provide time series of the methane mole fraction for a time period of 15 min. The AirCores are also controlled by the operator via WiFi. Therefore, the starting time of the air extraction of each system can be determined during the flight.

2.2.4. Radiation budget

For measuring the radiation budget, the following sensors were integrated on HELiPOD (see overview in **Table 5**): The standard pyranometers (CMP22, Kipp and Zonen, The Netherlands) and pyrgeometers CGR4 (Kipp and Zonen, The Netherlands), used for long-term measurements in surface radiation networks, were installed in both nadir and zenith orientations. Further, 6 silicium-based pyranometers (ML-01, EKO Instruments, Japan) with a wavelength range of 400–1,100 nm were integrated looking in the directions nadir, zenith, front, rear, left, and right. These sensors have a much higher temporal resolution in the order of microseconds and can be used for improving high-resolution attitude information based on solar geometry.

Zenith looking radiation measurements are influenced by the helicopter above the radiation sensors. Shading of direct sunlight is detectable by sudden decreases of the solar downward irradiance. The general influence of the helicopter can be estimated by comparing the measurements of the HELiPOD standing on the ground and in flight. Shading effects can also be modeled.

2.2.5. Surface properties

A summary of the surface sensors is shown in **Table 6**. Two infrared surface temperature sensors were applied. The cameras comprise different systems for documenting surface and sky properties and the visual impression:

Two 360° cameras and several visible and infrared cameras were installed in upward (zenith) and downward (nadir) orientations. The landing skids of the HELiPOD appear on the nadir looking camera images. These parts of the images can be masked out before the analyses (Sperzel et al., 2023).

A laser scanner (VLP-16, Velodyne, USA) was used for monitoring surface roughness. It provides a three-dimensional point cloud representation of the surrounding environment with a range of up to 100 m. For this, 16 rotating lasers cover a $\pm 15°$ vertical field of view and a 360° horizontal field of view around the rotation axis. Each laser fires approximately 18,000 times per second, which results in up to 300,000 data points per second for the entire sensor. The distance to any reflective surface is determined by measuring the time of flight that a laser pulse needs to return to the sensor. Apart from the distance measurements, the VLP-16 outputs a calibrated reflectivity measurement, the number of the firing laser, and the respective rotational angle. A separate GNSS receiver is connected to the VLP-16 that provides a pulse per second (PPS) signal and a predefined message in the format NMEA (National Marine Electronics Association). This allows for accurate timestamping in a resolution of microseconds.

2.3. Flexibility of sensor payload: Instrumental changes for planned and spontaneous campaigns

This section demonstrates the high flexibility of HELiPOD concerning the exchange of sensors upon requirements, and the quick integration of new sensors, mechanically, electrically, into the data acquisition and real-time display.

In 2022 for the METHANE-To-Go-Poland project, HELiPOD was deployed in the Upper Silesian Coal Basin in the Katowice area to investigate methane emissions and spatial methane distributions from coal mine ventilation shafts. This project was on behalf of the German Aerospace Centre (DLR) and funded by the United Nations Environment Programme (UNEP) under the International Methane Emissions Observatory program.

The following sensors and items were removed, as they were not required for the research focus, and to provide space and weight for the new sensors:

- two infrared cameras,
- thermodenuder,
- two CPCs and one OPC,
- surface temperature sensor KT19,
- discrete air samples and AirCores, and
- one 5-kWh battery (see Section 3.3).

In addition, on very short notice of few days, HELiPOD was operated above the Baltic Sea after the leaking of the NordStream pipelines to measure the methane emissions from the gas that was dissolved in the water column and later emitted into the atmosphere.

Around 1 month later, the flights above the Baltic Sea were repeated to investigate the emissions of methane stored in the surface water, with additional measurements of the methane isotopic composition. For this purpose, the instrumentation of HELiPOD was slightly modified. The Picarro G2401-m was replaced by a Picarro 2201-i for the follow-up campaign over the Baltic Sea, providing information on methane $\delta^{13}CH_4$ isotopy.

With the focus on methane emissions, it was required to measure the concentration complementarily with

a sensor of high temporal resolution and with a sensor of high accuracy. Additional sensors were integrated, as summarized in **Table 7**. The electrochemical sensors have a response time of 30–80 s (Schuldt et al., 2023). The aerosol sensor MA200 and the electrochemical trace gas sensors are characterized in Bretschneider et al. (2022). The ultrafast temperature sensor of the University of Warsaw is described in Kumala et al. (2013).

In addition, the Siemens LMS SCADS data acquisition unit with two 3-axis accelerometer PCB356B was integrated, one at the LI7700 sensor head and one at the device socket, and two PCB *xy* single-axis accelerometer lateral and vertical measuring at the LI7500A socket, obtaining the vibration spectra with a bandwidth of 25.6 kHz to assess the vibrational environment at HELiPOD (for more information, see Lampert et al., 2018).

The flexible power supply providing different voltage outputs makes it possible to integrate the new sensors in the electrical system. Several clients are available for different established data transfer protocols, which can be handled by the messBUS, and specific clients can be developed for new requirements. The adaptation of the real-time display to include new sensors can be done within few hours.

3. HELiPOD system basis

In this section, technical considerations for integrating sensors into the basic HELiPOD design concept are presented, accounting for different mission requirements. The main parts of the HELiPOD are described in detail, which are the data acquisition (Section 3.1), the thermal system (Section 3.2), and the electrical power system (Section 3.3).

3.1. Data acquisition system

As illustrated in **Figure 5**, HELiPOD is equipped with a large number of more than 60 sensors, from simple sensors to complex subsystems. The sensors are installed at various locations depending on the specific requirements of the sensors, such as undisturbed flow for open path sensors or unobstructed view to the surface for the laser scanner. A wide range of signal types are output by the sensors, ranging from analog signals at voltage levels of different orders of magnitude to sensor-specific digital data output. Transmission protocols may vary by sensor and data rates range from 0.5 Hz to 20 kHz. Precise timing is essential for most parameters, for example, when calculating the wind vector.

Systems like the VLP-16 laser scanner, the LI7500A, or the iNAT-M200/SLN-DA inertial navigation system provide measurement data directly via Ethernet, other sensors output data via USB and some cameras, such as the EOS-RP fish eye cameras, store their images locally on SD cards. The remaining sensors provide their readings in the form of voltages, currents, resistances, or a serial data stream. The various signal and data types in combination with the need for precise timing impose strong requirements on the components of the HELiPOD data acquisition system. For meeting these requirements, the data management units need different interfaces, high-performance data handling, and storage. In the current setup, the HELiPOD secondary unit handles all raw image data from the

cameras (approx. 400 GB per 3-h flight). All other data (approx. 100 GB per 3-h flight) are handled by the HELiPOD primary unit. The task is to collect the data in an appropriate way and store it, providing in-flight data access for system health monitoring and in-flight scientific decision-making. To handle the data without delay within the network, the switches are connected with a 10 Gbit per second connection to the data management units. In the latest setup, a third master switch was added between the primary and secondary for fast postflight data download. Synchronizing raw and partially processed data from various sources requires accurate timestamps.

Different time sources are used: absolute time provided by the GNSS (iNAT200 and JAVAD) receivers and PPS signals form the JAVAD receivers. The PPS signals stabilize time on the messBUS-ntp master, which is an independent network time protocol (NTP) server to stabilize the HELiPOD primary unit. The HELiPOD primary unit receives the time information and provides the NTP-time to other systems within the network, including the HELiPOD secondary unit, the laser scanner VLP-16, the LICOR7700, and, if available, the Picarro. After the MOSAIC campaign, the messBUS-ntp was replaced by a RaspberryPi4 operating as a self-sustaining NTP server, using the GNSS time and PPS of one JAVAD sensor and providing the NTP-time to all network devices. The time offset of the data management units is smaller than 1 μs. Thus, all data are stored properly timestamped and synchronized in postprocessing.

The challenges of noise infiltration, cross talk, and other parasitic effects on analog signals and long cable lengths as well as various electrical properties and data encoding of digital sensor outputs are addressed with the decentralized data acquisition system (called messBUS, components shown in **Figure 5**). The core idea is that both analog and digital sensor outputs are preconditioned and processed in the proximity of the sensors by dedicated client units. These are self-developed and self-built circuit boards that translate the sensor outputs into a consistent message protocol. As shown in **Figure 5**, each sensor is connected to the bus system via a respective client. Transmission times for the individual clients on the bus system are scheduled automatically by the messBUS master. A PPS signal from a JAVAD GNSS receiver is fed to the master unit, allowing for the distribution of precise time information throughout the system. This makes it possible to simultaneously timestamp incoming sensor readings while they are being captured by the clients. This is particularly important for the measurements of high temporal resolution.

The messBUS system works at an internal frequency of 100 Hz. Analog sensors are sampled with this frequency, and digital sensor data are handled with the configured data rate. Depending on mission-specific requirements, additional sensors can be included into the system by adding the respective client units at any position in the bus. The messBUS master automatically recognizes the new sensors and adapts the data transmission timing accordingly. A list of client types developed so far and their purpose is summarized in **Table 8**. **Figure 6** shows messBUS hardware located in the nose and center section of the HELiPOD.
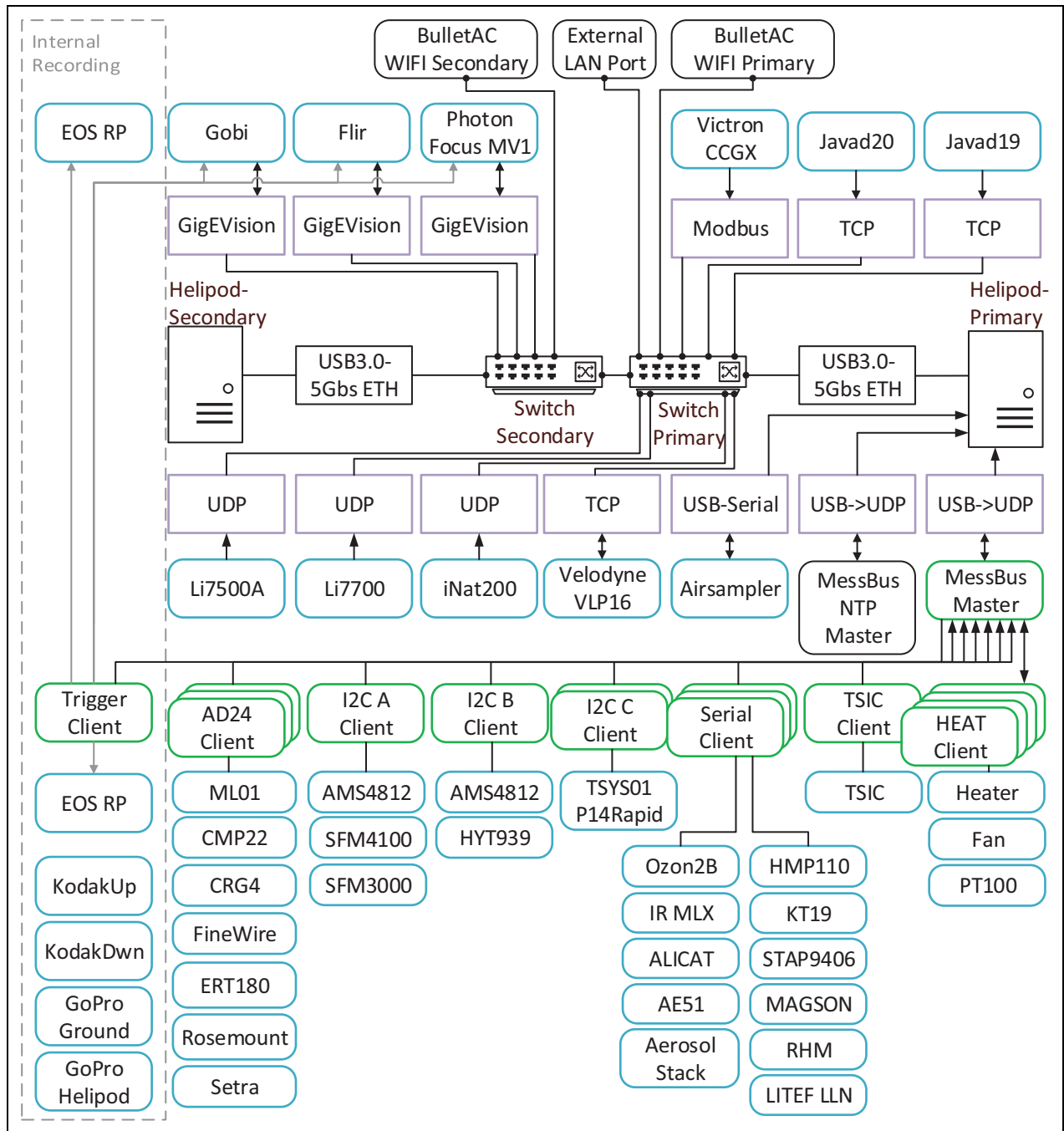
Figure 5. HELiPOD sensor and data acquisition hardware structure during the MOSAiC campaign. The illustration shows the data sources in blue connected to the primary and secondary data management unit. The connections using the local access network, a direct universal serial bus connection, or the messBUS system in green. The boxes in violet mark the used transmission protocols.

As shown in **Figure 5**, sensors vary in communication protocol, amount of data, and data frequency. Sensor packages also differ between deployments.

The Robot Operating System (ROS) is used to handle all incoming data in the storage units. It is a centralized data distribution system running on ubuntu Linux and scalable hardware from RaspberryPi for drones to high-performance computation units (like within the HELi-POD). It is based on a "publish and subscribe" principle. That means new data provided by a data publisher are written to the working memory, triggering the read

function of all subscribers that are registered for these messages. The data rates depend on the provided data rate (e.g., 100 Hz for analog messBUS sensors or 40 Hz for the Li7700). Higher data rates, for example, raw accelerations measured by the iNAT200, are stored on internal memory due to the limited interface performance. Nevertheless, the iNAT provides real-time processed navigation data to the ROS system. The ROS record module stores the maximum data rates. The subscribes of the live system monitor use reduced data rates between 1 and 10 Hz to reduce the system load. **Figure 7** shows the HELiPOD ROS

system configuration and distribution. The ROS core master is the central management process started during boot process. Each data providing system is connected to a ROS node—a "Python" or "C++" software module running as an independent process. The nodes handle the individual connection to the system, streaming raw data to a backup file, translating and time stamping the incoming data to custom defined messages, and publishing them within the ROS core. The ROS nodes of the HELiPOD-Secondary unit (see **Figure 7**) are connected to the ROS core via a remote ROS Launch instance piping all data threw the network to the ROS core in a bidirectional way. Additional ROS nodes are running as decoder services subscribing to incoming data to decode serial data or calculate important data and publish them for in-flight monitoring and postflight quickviews.

The ROSbag module enables the recording of all or selected data, by subscribing to the defined data and streaming it to a binary ROSbag file. It consists of the binary data and the header information describing all recorded messages down to basic data types. The ROSbag module also allows a playback of the recorded files and allows to identify bugs or to extract quicklook data. For postflight data analysis, MATLAB and python interfaces

Table 8. Overview of clients developed for the mess-BUS system in HELiPOD

Client	Purpose
A/D Client	A/D conversion of analog sensor outputs
I²C Client	Sensors with I²C interface
Serial Client	Sensors with serial interface
TSIC Client	TSIC-Sensors with ZACWire protocol
Heating Client	Control of heating system
Trigger Client	Trigger pulses for cameras

allow easy access to all the data (see Section 3.4). The ROSbridge-server module is an additional function that is used to enable a websocket interface that allows to publish and subscribe data within the HELiPOD network via Javascript (JS). JS facilitates easy access of the data with a browser-based application running on the operator station in the helicopter (**Figure 8**—top right).

During the MOSAIC campaign, a StatusMonitor view (see **Figure 8**—bottom) was used to display the system state, including battery state, data management performance, sensor system status, and a control interface for the heaters and the gas probe system. A DataMonitor view mode shows real-time measurements and monitors sensor state. A more sophisticated development view and live compressed images of the cameras were also implemented. Additionally, a radar altimeter view was developed and provided to the pilot via a 7-inch display. The operator can define a reference altitude, and the pilot sees the difference between reference and radar altitude as a number and graphically as a vertical bar. This facilitates low-altitude legs and level flight at high altitudes. Since 2022, the MissionMonitor view was implemented, showing map position and coloring the flight path with selected data and a flexible scale (e.g., methane mole fraction along the flight path). Furthermore, a time plot and various altitude plots show mission relevant measurement data. Parameters and scales can be modified, depending on the research task and the current observations. A screenshot-comment function is included to enable capturing personal observations of the operator easily, which is available in the quicklook data.

3.2. Thermal system for instrumentation temperature control
3.2.1. General overview of thermal system
A sophisticated thermal system was necessary for different reasons: Several sensors and sensor systems (e.g., CPCs, black carbon sensor, and the Picarro trace gas sensor) should be kept at moderate temperatures to ensure their
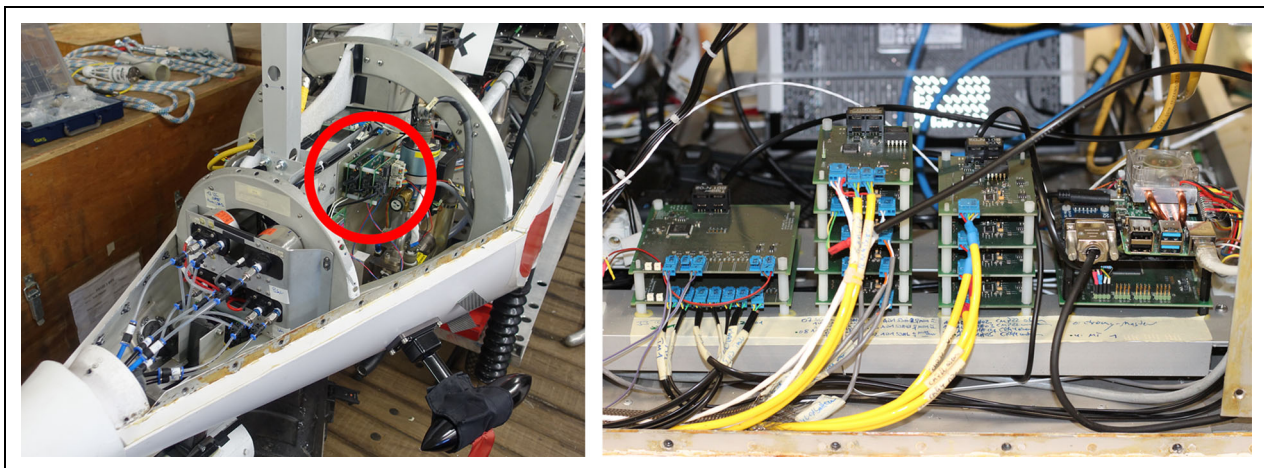

Figure 6. Internal view of HELiPOD, showing messBUS hardware for data acquisition. Left: The analog outputs of the pressure sensors in the nose section of the HELiPOD are digitized by the marked set of A/D clients located close to the sensors. Right: Additional client units in the center section. The circuit board at the bottom on the right-hand side is the bus master unit.
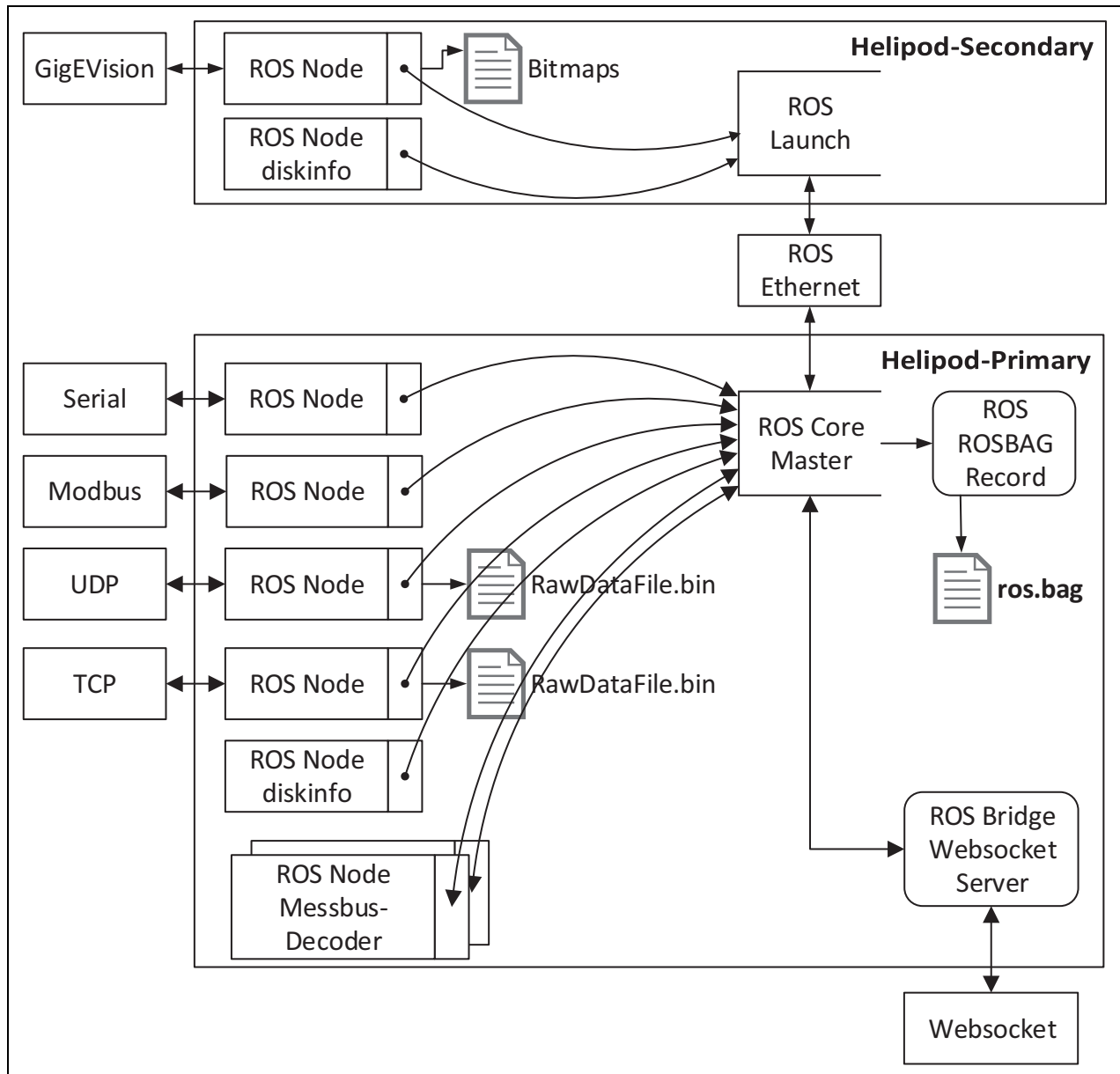
Figure 7. HELiPOD data acquisition software structure applied for the MOSAiC campaign. The illustration shows the Roboter Operating System (ROS) and exemplary the distribution of ROS interface nodes for different kinds of sources on the primary and secondary data management units.

smooth operation. Furthermore, sensor calibrations should be done at their deployment temperature, so room temperature is most favorable. Finally, most instruments are sensitive to temperature gradients, and in particular, rapid changes of temperature should be avoided, even within the specified operational temperature range. The specific criteria for internal temperature control depend on the instrument package (see Section 2.2), but the nominal target temperature is 18°C. As the sensors are either placed directly in the air flow or have the inlet at the front section (see **Figure 3**), the insulation and heating do not have an impact on the measurements.

For the MOSAiC expedition, a lowest deployment temperature of −40°C was assumed to calculate the requirements for insulation, heaters, and power supply. The basic concept was to retrofit an insulation to the aluminum

structure of the HELiPOD and integrate well-regulated electrical heaters directly downstream of the 4 fans. As some sensors require manual handling before each flight and for maintenance reasons, the insulation was designed in a way to allow easy access to the payload.

The heat flow calculation was based on a one-dimensional three-part model that was scaled to the surface size of the HELiPOD (**Figure 9**). The first part represents the original aluminum structure that was insulated with a 20-mm-thick commercial insulation foam and covered with a 3-mm-thick semisolid polyvinyl chloride foam to achieve a robust surface. The second part represents heat bridges, that is, parts of the HELiPOD where proper insulation could not be implemented, like the skid dampers. This part was calculated to estimate the importance of detailed insulation in the effort-to-benefit discussion.

Figure 8. Remote WiFi access to the HELiPOD during flight. A specially developed user interface enables to monitor the current state of the whole system and sensors. Life sensor data are displayed allowing operational decision-making. A control of sensors and temperature management is given.

Both parts represent conductive heat flow combined with convective heat flow at both sides. A third part represents the heat lost due to in-flowing cold air because of inevitable small leaks and inflow due to pressure increase during descent flight (advective heat flow). This calculation was also performed to quantify the sensitivity and thus the effort required to prevent leaks and the additional energy consumption during descent flight. The thermal modelling was based on experience with designing, operational data, and postcampaign experimental and theoretical assessment of the thermal budget of the UAS ALADINA (Lampert et al., 2020a).

The total heat flux ϕ_{total} is calculated for the surface of the HELiPOD and is thus equal to the total power needed to obtain the desired temperature difference. It consists of combined conductive and convective heat fluxes through the structure $\phi_{\text{structure}}$, an inflow of outside air due to leaks ϕ_{leaks}, and during descent flight ϕ_{descent}:

$$\phi_{\text{total}} = \phi_{\text{structure}} + \phi_{\text{leaks}} + \phi_{\text{descent}}. \tag{2}$$

For calculating the first term, the thermal resistance R $[K/W]$ is used:

$$\phi_{\text{structure}} = \frac{\Delta T}{R_{\text{total}}}, \tag{3}$$

where ΔT is the air temperature difference between the inside and the surrounding. The total thermal resistance combines a solid-state heat conduction portion and a convection portion due to the air flow at both sides of the HELiPOD shell:

$$R_{\text{total}} = R_{\text{conductive}} + R_{\text{convective,inside}} + R_{\text{convective,outside}}. \tag{4}$$
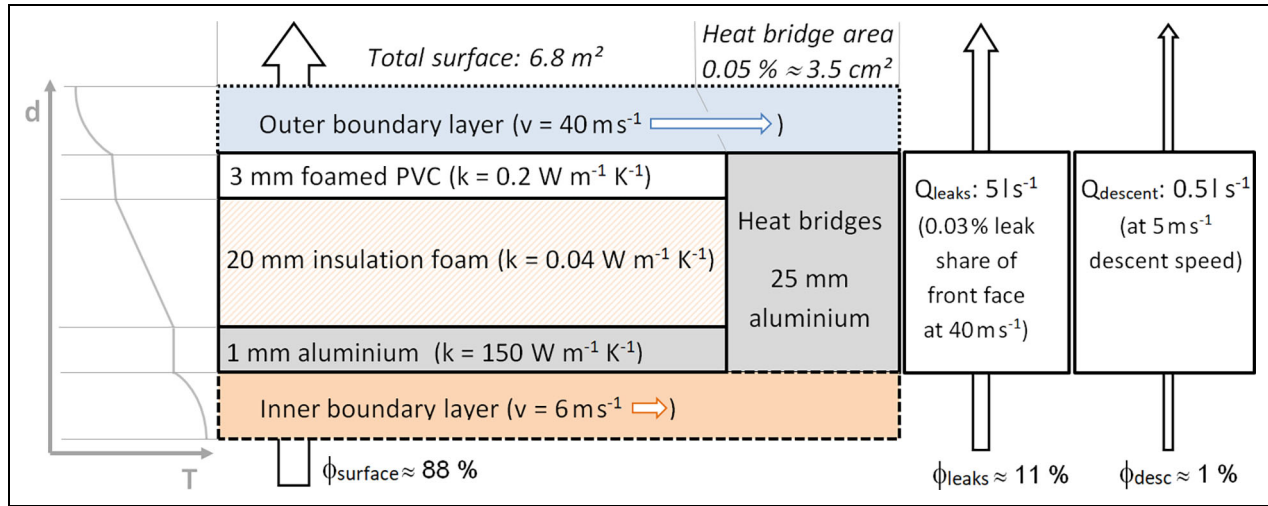
Figure 9. Thermal model including numbers, dimensions, and outcome. The temperature graph on the left shows the qualitative progression between the inside and outside air temperature.

The heat conduction is calculated using Fourier's law

$$\phi = -k\frac{\mathrm{d}T(x)}{\mathrm{d}x} = -k\frac{\Delta T}{d}, \tag{5}$$

where k is the thermal conductivity. The material-specific thermal conductivity for each homogeneous layer R_i is used to calculate the total thermal heat resistance using the layer thickness d and the total surface A:

$$R_\mathrm{i} = \frac{d}{k \cdot A}. \tag{6}$$

It is calculated as parallel configuration to combine the well-insulated part and the heat bridge part,

$$\frac{1}{R_\mathrm{total}} = \frac{1}{R_\mathrm{insulated}} + \frac{1}{R_\mathrm{bridges}}, \tag{7}$$

while the thermal heat resistance of the layers of the well-insulated hull areas is calculated as serially arranged:

$$R_\mathrm{insulated} = R_\mathrm{aluminum} + R_\mathrm{insulationfoam} + R_\mathrm{outershell}. \tag{8}$$

The convective heat resistance assumes turbulent flow and is calculated using standard formulas from thermodynamics formula collections. It must be considered separately for the inside (depending on the fan speed setting) and the outside (depending on flight speed).

The heat flow because of leaks ϕ_leaks and inflow during descent flight ϕ_descent is calculated in the same way:

$$\phi_\mathrm{leaks/descent} = Q_\mathrm{leaks/descent} \cdot c \cdot \Delta T, \tag{9}$$

where Q is the volume flow and c is the specific heat capacity.

With the chosen dimensions, shares and parameters (see **Figure 9**) a ratio of 0.88:0.11:0.01 results for the terms in Equation 2. The total heat flux is calculated as 50 W K^{-1} for in-flight conditions and 28 W K^{-1} on ground. Thus, the power consumption of the measurement system of about 500 W (measured consumption) heats the inside of the HELiPOD during flight by 10 K above the outside air temperature and by 18 K on ground without the need of

additional heating. Therefore, during ground operation, the possibility of an inside overheating must be kept in mind even in Arctic outside conditions.

To provide the required heating power of roughly 2,400 W at $-40°$ outside air temperature, four controlled resistor heaters were integrated, each approximately 1 kW. Several safety criteria were implemented: Temperature limits and gradients are observed and regulated with the heater control software, operator override can shut down each heater independently, and temperature switches on each heater will cut off power above certain temperature limits.

To achieve a homogeneous temperature inside the HELiPOD, which is also a basic assumption of the one-dimensional thermal model, four strong air circulation fans are installed, nominally capable to circulate the inside volume once per second at maximum fan speed (**Figure 10**).

A thermal image camera was used to check the HELiPOD for heat bridges (**Figure 11**). To observe the temperature distribution, 24 temperature sensors were installed at different locations inside, and the data were available to the operator during the flight to monitor the internal conditions (**Figure 11**). Temperature measurements of the outside air are available from the standard measurement set.

The power consumption for the observed internal temperature distribution as a function of outside temperature is 10% less than modeled. While differences in temperature distribution up to 3 K were measured within HELiPOD, this distribution is very static within the fuselage.

3.2.2. Changes for METHANE-To-Go

During the summer campaign, outside air temperature was sometimes above 30°C. As no cooling device was installed, an additional fan was used to flush outside air into the HELiPOD for cooling, achieving an inside air temperature level not more than 1 K above the outside air temperature.

3.2.3. Future development

An active cooling system is needed for deployment in warmer areas to keep the inside air temperature below
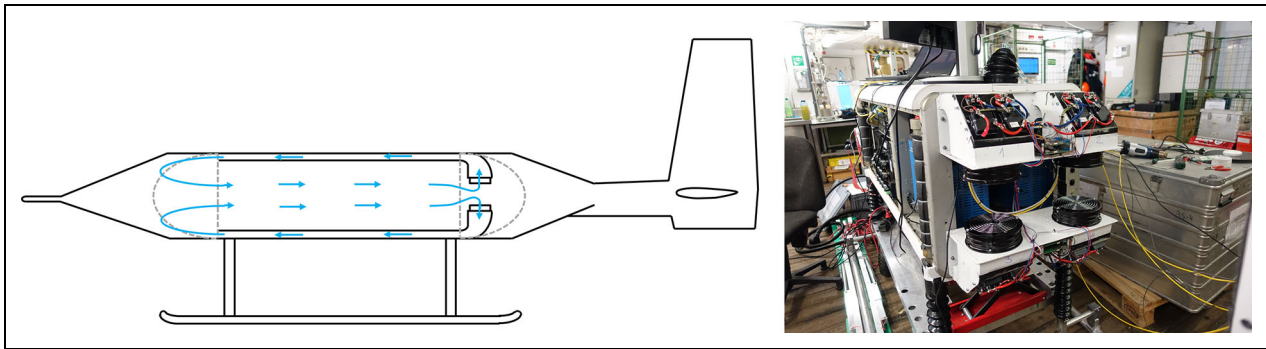
Figure 10. Internal air circulation and heater. Left: The air inside is circulated by four fans through structurally integrated chambers at the top and the bottom of the center section. Right: Four fan-heater units are installed at the rear end of the center section.
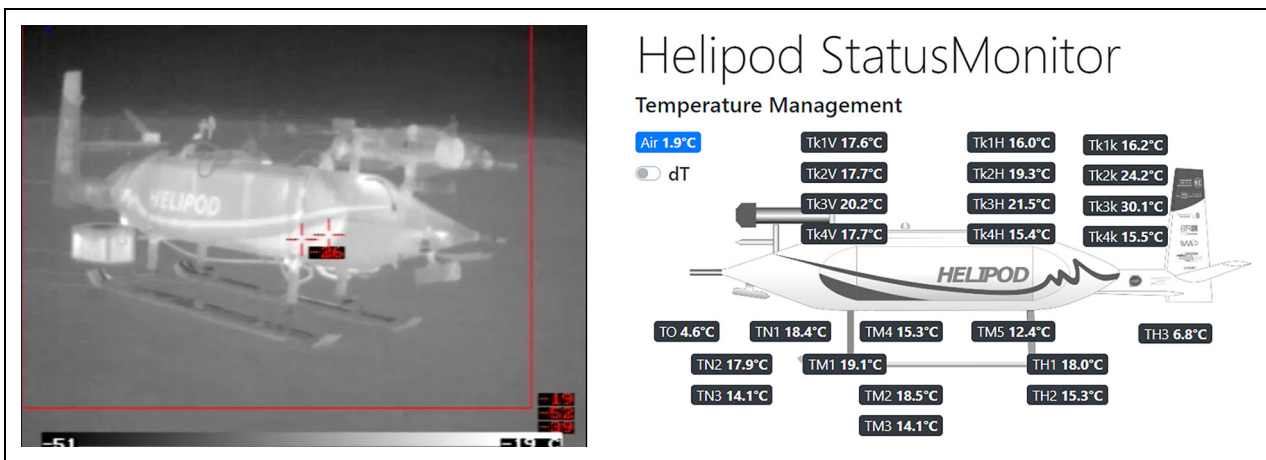

Figure 11. Helipod thermal management. Left: An infrared camera was used to check the HELiPOD heat signature. Right: The most crucial internal temperature data are presented to the operator in real time.

the outside air temperature. Implementing the heat pump principle for cooling purposes can also reduce the power needed for heating, compared to the current resistor heater. A proper insulation is also favorable for operation in hot outside conditions. A higher degree of automation of the heat management should be implemented to reduce the operator's workload.

3.3. Electrical power system

The electrical power system was completely redesigned to supply all devices according to the respective demands and to handle the system efficiently with a limited set of switches (**Figure 12**). A stand-alone battery system in HELiPOD was chosen, as electrical connections to the helicopter would raise the need for aviation certified interfaces, and the excess electrical power of the helicopter is barely sufficient for the heating demands. A disadvantage of the battery-based approach is reduced space and weight for the scientific payload inside the HELiPOD. To ensure safety, the basic principles of aircraft wiring and fusing were applied, for example, the sockets and plugs were chosen in a way that they cannot be exchanged accidentally, and cables were marked with different colors and unique identifying codes, which correspond to a specific socket/plug pair.

The power consumption of the entire scientific payload of approximately 490 W (measured for sensors and data acquisition) and the required heater output for keeping the inside temperature in an acceptable range defined the needed battery capacity for a given maximum operation of 2.5 h during the MOSAiC expedition (maximum 2-h flight time of the helicopter plus some ground handling time as buffer). In addition, a ground-power hookup had to be designed for harsh Arctic conditions, which can be disconnected quickly directly before the flight and reconnected after landing.

As a compromise of weight, scalability, availability, and costs, a commercial system from Victron Energy (The Netherlands) was used, including the "high-energy" batteries, which were only recently available on the market. The system includes a master, charger, DC/DC-converters, battery protect modules (fuses), and a control unit. The power system data were fed into the data acquisition as well, so the operator is aware of the power supply state. The commercial off the shelf system can be seen as proven by practice. The system deployed during MOSAiC hosted 2 batteries of 5 kWh each. Only DC voltages were provided using DC/DC converters at 24, 12, and 5 V and directly from the batteries (nominal 25.6 V).
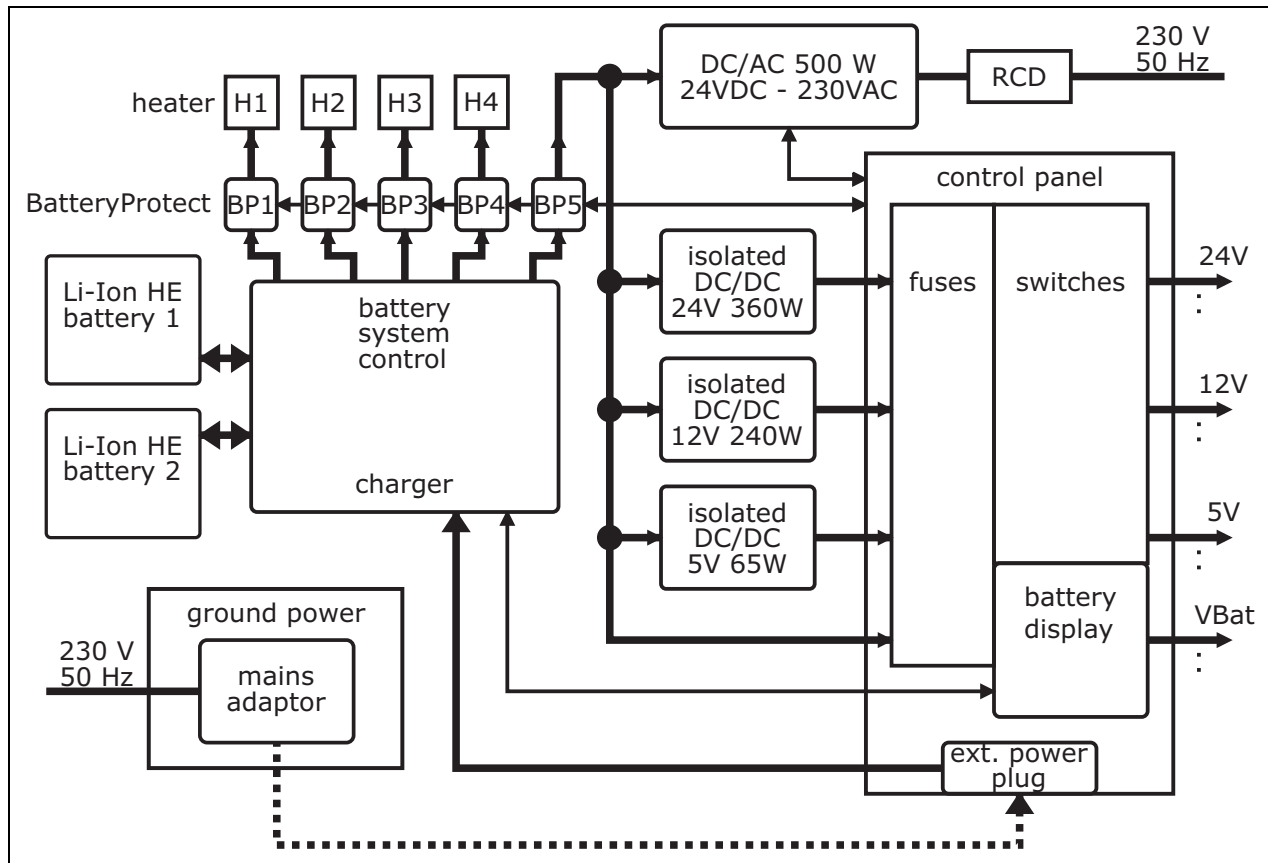
Figure 12. HELiPOD power supply system.

For the METHANE-To-Go campaign, only half of the battery capacity was installed (5 kWh). The additional weight and space allowance were used to accommodate Picarro G2401-m and G2210-i analyzers and associated pumps. To provide power supply to the Picarro subsystem, a DC/AC-converter was added (Section 2.3).

The reduced battery capacity was still sufficient to supply the system for a flight time of up to 3.3 h requiring about 50% of the battery capacity, when air temperatures are above 15°C and ground support is conducted on external power. The reserve capacity was significantly reduced in November during flights over the Baltic Sea at air temperatures of around 0°C with 25% capacity left after 2.5-h flight, as the heating needs were significantly higher. On a panel, several switches were used to control groups of instruments with aviation fuses for each instrument. The system can be operated completely via this control panel, including switching on and off recording and shutdown of the data acquisition (**Figure 13**).

3.4. Data postprocessing
3.4.1. Data processing chain
The data processing chain from the raw data to the final data requires several steps:

- reindex raw files stored by Robotic Operation System to reorder the data by timestamps and write header information,
- convert raw data from the binary ROSbag format to a format used for postprocessing (in this case MATLAB),

- check for potential decoding errors,
- check and correct timing issues,
- offline postprocessing of navigation data (see Section 3.4.2),
- decode and convert data stored separately, for example, laser scanner,
- check device internally stored data with centrally stored data,
- synchronize all data sets,
- resample and upsample to 100 Hz by spline interpolation,
- apply calibration factors,
- compute derived parameters from multiple sensors, for example, the 3D wind vector, and
- apply physical correction methods, for example, from flight calibration maneuvers

After each step, plausibility checks and comparisons are performed.

3.4.2. Postprocessing of navigation data
Position and attitude of the HELiPOD are derived from the data recorded by the inertial navigation unit iNAT-M200DA-SLN. The GNSS and inertial postprocessing were performed using the Inertial Explorer 8.70 software (NovAtel Inc., Canada). Advanced methods such as precise point positioning and tightly coupled sensor data fusion have been applied to achieve highly accurate positioning solutions. The resulting data set contains supplementary data, for example, velocities, accelerations, a quality number, or the
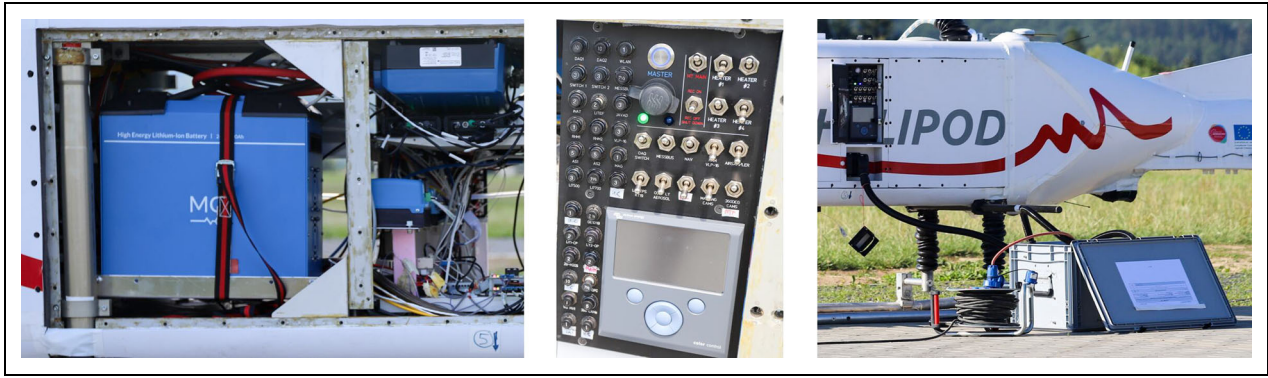
Figure 13. The HELiPOD power supply system. Left: Li-ion high-energy battery with battery system control and DC/
DC converter. Middle: Control panel. Right: Ground power connection.

sun's azimuth and elevation. The positioning solution in combination with the sensor measurements, laser scanner data, and camera images provides a comprehensive and georeferenced database for further research.

3.4.3. Complementary filtering

HELiPOD provides redundant measurements from multiple sensors for deriving data products of enhanced quality and as a backup for single sensor failure. Complementary filtering combines the advantages of different sensor types, for example, a slow sensor with higher accuracy and a drifting sensor with high temporal resolution. Typically, a low-pass filter is applied on the slow sensor distorted with noise and a high-pass filter for the fast sensor, which might suffer from drifting in time. When a reconstruction filter (inverse filtering using the sensors' inherent transfer function from the physical quantity to the measurements) is applied to a slow sensor in order to reduce time lag, a significant noise amplification will occur, which is subsequently eliminated during the complementary filter process (Bärfuss et al., 2018). With LP denoting a low-pass filter and HP denoting a high-pass filter, the complementary measurement $SensorsFused$ can be calculated as

$$SensorsFused = LP(Sensor_1) + HP(Sensor_2), \qquad (10)$$

which combines the high-frequency component of the fast sensor with the low-frequency component of the slow sensor. This is achieved by respecting the premise that the transfer functions used in the complementary filter process for sensors to be fused must sum up to 1. The combination of a simple first-order transfer function for a high-pass filter and a first-order low-pass filter with an identical time constant denotes a power as well as phase complementary filter set, as it fulfills the requirement of a transfer function sum of

$$G(s) + H(s) = \frac{1}{1 + T_1 s} + \frac{T_1 s}{1 + T_1 s} = 1, \qquad (11)$$

with the transfer function $G(s)$ for the low-pass filter and the transfer function $H(s)$ for the high-pass filter, both with the time-constant T_1. Here, s denotes the Laplace factor. To fuse three sensors measuring the same physical quantity, the complementary technique can either be

stacked for the increasingly fast responding sensors $Sensor_1$, $Sensor_2$, and $Sensor_3$ such as

$$SensorsFused_{1,2,3} = LP_2(SensorsFused_{1,2}) + HP_2(Sensor_3),$$
$$(12)$$

with

$$SensorsFused_{1,2} = LP_1(Sensor_1) + HP_1(Sensor_2), \qquad (13)$$

where the crossover frequency f_{LP_1,HP_1} is lower than the crossover frequency f_{LP_2,HP_2}, or a bandpass function $I(s)$ can be developed using

$$
\begin{aligned}
I(s) &= 1 - G(s) - H(s) \\
&= 1 - \frac{1}{1 + T_1 s} - \frac{T_2 s}{1 + T_2 s}, \\
&= \frac{(T_1 - T_2)s}{(1 + T_1 s)(1 + T_2 s)}
\end{aligned}
\qquad (14)
$$

with the time constant T_1 for the low-pass filter and T_2 for the high-pass filter. The resulting bandpass transfer function equals an amplified cascade of a high-pass and a -bandpass filter

$$I(s) = K \cdot H(G(s)) \qquad (15)$$

with an amplification factor $K = \frac{T_2 - T_1}{T_2}$.

This technique is applied in the HELiPOD to fuse the different temperature sensors as well as the moisture readings of the different humidity sensors. Typical crossover time constants to fuse platinum wire temperature sensors with industrial thermistors are around 10 s … 60 s. For moisture measurements, crossover frequencies have to be investigated depending on the instruments deployed and the integration type, as, for example, capacitive humidity sensors suffer from substantially increased response times in cold environments depending further on the flow speed around the sensors.

4. Operational experiences during MOSAiC and METHANE-To-Go

The operation of a system like HELiPOD includes the aspects of logistics for transporting the system from the homebase to the deployment site, onsite logistics, and flight operations. Understanding and dealing with these aspects are essential for a safe and efficient deployment.

Table 9. Overview of the 5 measurement flights that were performed with HELiPOD during the MOSAiC expedition

Flight	Date	Takeoff	Landing	Pattern	Scientific Focus
1	May 10, 2020	11:30	12:31	HL approx. 20 km	Impact ship activity
2	June 30, 2020	14:42	16:31	VP 1,500 m, HL approx. 40 km	Persistent NPF
3	July 1, 2020	12:34	14:20	VP 1,500 m, HL approx. 40 km	Persistent NPF
4	July 22, 2020	11:56	12:53	HL approx. 50 km	Shallow ABL
5	July 22, 2020	13:16	14:19	HL approx. 65 km	Shallow ABL

The takeoff and landing times are indicated in UTC. The flight pattern consisted of horizontal legs (HLs) with different distances to *Polarstern* but was performed at a constant height, and 2 vertical profiles (VPs) in the atmospheric boundary layer (ABL) were operated with a maximum altitude of 1,500 m on June 30 and July 1, 2020, when a persistent new particle formation (NPF) event was observed at the ship. MOSAiC = Multidisciplinary drifting Observatory for the Study of Arctic Climate.

Table 10. Overview of the HELiPOD mission flights performed during the METHANE-To-Go-Poland field experiment in Poland (Upper Silesian Coal Basin) in June 2022

Flight	Date	Takeoff	Landing	Target Region	Scientific Focus
1	June 13, 2022	10:35	10:45	BB area	HELiPOD training
2	June 13, 2022	10:50	11:40	BB waste water fac.	Test flight
3	June 14, 2022	09:30	11:40	Sz Shaft IV	CH_4 mass flux ventilation shaft
4	July 14, 2022	14:20	17:30	Sz Shaft IV	CH_4 mass flux ventilation shaft
5	June 15, 2022	10:15	13:35	Sz Shaft IV, Pn area	CH_4 mass flux ventilation shaft
					TROPOMI satellite validation
6	June 16, 2022	09:55	12:35	Sz Shaft IV	CH_4 mass flux ventilation shaft
7	June 18, 2022	13:16	14:19	Sz Shaft IV	CH_4 mass flux ventilation shaft
8	June 18, 2022	14:10	16:40	BA Shaft IX	CH_4 mass flux ventilation shaft
9	June 20, 2022	08:05	11:20	Pn Shaft V	CH_4 mass flux ventilation shaft
10	June 21, 2022	17:10	20:20	BA Shaft IX	CH_4 mass flux ventilation shaft
11	June 22, 2022	08:30	09:00	BB area	Technical flight for wind calibration
12	June 22, 2022	10:30	13:50	BA Shaft IX	CH_4 mass flux ventilation shaft
13	June 23, 2022	08:05	11:25	Pn Shaft V	CH_4 mass flux ventilation shaft

The takeoff and landing times are indicated in local time. BB refers to the city Bielsko-Biala, fac. To the facility, Sz to the Szczyglowice, Pn to the Pniowek, and BA to the Brzeszcze-Andrzej coal mine ventilation shaft.

HELiPOD was disassembled and packed into boxes of dimensions and weight that can be handled manually for shipment to the remote Central Arctic. The mechanical and electrical reassembly was done on the *Polarstern*. For safety reasons, it was decided to operate the HELiPOD only from the floe and at least 100 m away from *Polarstern* with more safety margin compared to limited space on the helideck. This led to additional logistical efforts before an operation was possible.

Onboard *Polarstern*, the HELiPOD was transported with the help of a cart with large wheels. Then, HELiPOD was craned from the ship by the ships' crew. On the ice, HELiPOD was transported to a safe distance from the ship on ski and was either moved manually or by a skidoo.

Due to the complex operational procedures, it was not possible to respond to weather events on short notice. The weather allowed less flights with progressing melting season, which was accompanied by frequent low-level cloud coverage, for instance, shown by the reduced mean cloud base height between June and August 2020 in Creamean et al. (2022). A total of 5 flights were performed during MOSAiC (see **Table 9**). The main flight pattern of **Figure 2**, left, was applied. The scientific focus of the ongoing data evaluation is on the following aspects:

- variability of atmospheric conditions in the surroundings of the *Polarstern*,
- variability of sea ice conditions,
- variability of the radiation budget,

Table 11. Overview of the HELiPOD mission flights performed during the METHANE-To-Go-Poland field experiment in Poland (Upper Silesian Coal Basin) in October 2022

Flight	Date	Takeoff	Landing	Target Region	Scientific Focus
1	October 10, 2022	12:30	15:30	Pn area	TROPOMI satellite validation
2	October 11, 2022	16:30	18:15	BA Shaft IX	CH_4 mass flux ventilation shaft
3	October 12, 2022	11:10	14:20	Pn Shaft V	CH_4 mass flux ventilation shaft
4	October 13, 2022	13:40	16:20	BA Shaft IX	CH_4 mass flux ventilation shaft
5	October 14, 2022	10:10	13:20	Pn Shaft V	CH_4 mass flux ventilation shaft
6	October 16, 2022	12:10	15:10	AP Shaft V	CH_4 mass flux ventilation shaft
7	October 17, 2022	10:00	13:15	AP Shaft V	CH_4 mass flux ventilation shaft
8	October 17, 2022	14:30	15:40	BB airfield	Controlled CH_4 release experiment
9	October 18, 2022	11:25	12:25	BB airfield	Controlled CH_4 release experiment

The takeoff and landing times are indicated in local time. BB refers to the city Bielsko-Biala, Pn to the Pniowek, BA to the Brzeszcze-Andrzej, and AP to the Agnieszka-Powietrzny coal mine ventilation shaft.

- variability of trace gases,
- variability of aerosol properties, and
- interaction of the abovementioned parameters.

The HELiPOD mission flights performed during 2 METHANE-To-Go-Poland field experiments in Poland in June and October 2022 (in summary 22 flights) were targeting methane emissions from single coal mine ventilations shafts in the Upper Silesian Coal Basin (**Tables 10** and **11**). The main flight pattern of **Figure 2**, right, was applied. These shafts are known to be major contributors to anthropogenic methane emissions in Poland and have therefore been selected by UNEP as potential methane mitigation targets. Such CH_4 measurements in combination with HELiPOD wind measurements are needed to determine the methane mass fluxes from the single ventilation shafts (Förster et al., n.d.).

In a next step, these methane fluxes are compared to production data from the coal mine owners to better understand how reliable these data are as input for current CH_4 emission inventories. In addition, such airborne CH_4 measurements can be used to evaluate satellite measurements (as TROPOMI) to reveal problems and failings of satellite-based CH_4 retrievals. To prove the novel measurement setup and concept, two controlled CH_4 releases were performed during the field phase period in Poland.

Targeted measurements, as during METHANE-To-Go-Poland, will help the energy industry and governments prioritize their CH_4 emission mitigation strategies, actions, and policies in the future.

5. Conclusions and further development

This article presents the design and technical details of the helicopter-borne probe HELiPOD for atmospheric research. The new design concept is presented here based on the deployment during the MOSAiC expedition in 2020 and as deployed during different METHANE-To-Go-Poland campaigns in 2022. The focus of the MOSAiC campaign was to investigate the interaction between the Earth System Compartments in the high Arctic. The focus of the METHANE-To-Go campaigns was to study anthropogenic emissions and the spatial distribution of methane.

HELiPOD is a unique tool, providing complementary information on atmospheric and surface properties relevant to a range of research objectives with high temporal resolution. HELiPOD is able to fly at low altitudes and close to observational targets, at a slower speed than the typical manned research aircraft, yielding highly resolved measurements.

Another significant advantage of HELiPOD is that it is fully self-contained, meaning that no other external power supply is needed and the data can be observed by the operator in the helicopter in real-time via WiFi. In addition, apart from a rope, no further connections between the helicopter and the system are necessary. From the helicopter's perspective, carrying the HELiPOD is a conventional external sling load operation, but due to the large payload weight, it requires skilled pilots.

Due to its payload capacity, the HELiPOD can carry a large amount of measurement technology. The internal messBUS system allows an accurate synchronization of the sampled data and facilitates integration of additional equipment, so that sensors on board can be easily extended or replaced according to the requirements of planned flight missions.

The HELiPOD system is continuously being improved, and the operating procedures refined. Two operators on site are mandatory to ensure successful campaigns. The efficiency of operations from the ship with interdependent processes has to be carefully planned for the next missions. Procedures for postprocessing HELiPOD data will be further developed toward higher automation for future applications.

Locations of future applications are not limited to places in moderate or polar climate zones. When the outside temperature is significantly higher than the required inner compartment temperature, the onboard heaters can be replaced by a cooling unit to avoid the risk of

a potential overheating and to assure a constant inner temperature range for the optimized work flow of the integrated sensors.

Data accessibility statement

The data obtained with HELiPOD during the campaigns have not yet been fully published but are in preparation or have been submitted for publication:

- Sperzel, TR, Jäkel, E, Lampert, A, Birnbaum, G, Pätzold, F, Neckel, N, Rosenburg, S, Fuchs, N, Wendisch, M. 2023. Surface type classifications from helicopter-borne imagery during the MOSAiC expedition. PANGAEA. https://doi.org/10.1594/PANGAEA.958997.
- Sperzel, TR, Jäkel, E, Lampert, A, Birnbaum, G, Pätzold, F, Neckel, N, Rosenburg, S, Fuchs, N, Wendisch, M. 2023. Helicopter-borne solar broadband irradiance measurements from the MOSAiC expedition. PANGAEA. https://doi.org/10.1594/PANGAEA.958999.
- Sperzel, T, Jäkel, E, Pätzold, F, Lampert, A, Niehaus, H, Spreen, G, Rosenburg, S, Birnbaum, G, Neckel, N, Wendisch, M. 2023. Broadband albedo measurements and surface type classification from HELiPOD and helicopter during MOSAiC. *Scientific Data.* https://doi.org/10.1038/s41597-023-02492-6.
- Pätzold, F, Bretschneider, L, Schlerf, A, Bollmann, S, Asmussen, MO, Bärfuss, KB, Harm-Altstädter, B, Käthner, R, Wehner, B, Pilz, C, Düsing, S, Herber, A, Sachs, T, Bestmann, U, Hanke, D, Sperzel, T, Jäkel, E, Wendisch, M, Wiekenkamp, I, Lampert, A. Multidisciplinary observations with the helicopter borne probe HELiPOD during the MOSAiC Expedition on Leg 3 and Leg 4, 2020 (Level 1), in preparation for PANGAEA.
- Asmussen, MO, Pätzold, F, Bretschneider, L, Harm-Altstädter, B, Bärfuss, KB, Bollmann, S, Schlerf, A, Sperzel, TR, Jäkel, E, Käthner, R, Pilz, C, Wehner, B, Sachs, T, Sauer, D, Herber, A, Jurányi, Z, Lampert, A. Overview of the measurements of the helicopter borne probe HELiPOD during the MOSAiC expedition, in preparation for *Earth System Science Data.*
- Bollmann, S, Hanke, D, Pätzold, F, Bretschneider, L, Bärfuss, K, Sandgaard, J, Bestmann, U, Lampert, A. Approaches to determine the surface roughness of Arctic sea ice using a laser scanner onboard the helicopter-borne measurement system HELiPOD, in preparation for *Annals of Glaciology.*
- Förster, E, Huntrieser, H, Lichtenstern, M, Pätzold, F, Bretschneider, L, Lampert, A, Necki, J, Jagoda, P, and Roiger, A. Quantifying methane emissions from industrial activities: A novel helicopter-borne application, in preparation for *Atmospheric Measurement Techniques.*

Supplemental files

The supplemental files for this article can be found as follows:

An example of the operation documented with the 360° camera is provided as video supplement.

Competing interests
The authors declare no competing interests.

Author contributions
FP realized the concept of the modernization of HELiPOD, coordinated all activities during the modernization, participated with HELiPOD in the Multidisciplinary drifting Observatory for the Study of the Arctic Climate (MOSAiC) expedition, and wrote the main text. SN and BB developed the messBUS system for distributed data acquisition and adapted it to the needs of HELiPOD in the preparation phase and during the mission. LB developed the Robot Operating Systems for data handling. KB realized the electronics hardware, tested the navigation sensors and provided online support for data acquisition during the campaign. SB included the cameras into HELiPOD and coordinated the technical support activities during the MOSAiC expedition. MOA supported the mechanical integration and shipping. AS developed the hardware for the measurement system and tested the electronics boards. BH-A and BW developed the concept for integrating the aerosol sensors into HELiPOD. PH provided internal and additional cofunding for the project. BGvdW performed the calculations of the rotor downwash geometry. AL and TS developed the concept of applying HELiPOD during MOSAiC. TS participated in the MOSAiC expedition. AL coordinated logistical, administration, and permission issues. AR and HH developed the concept of applying HELiPOD for METHANE-To-Go-Poland and Nordstream and organized and participated in the campaigns. All authors contributed to the text and revised the manuscript.

References

Altstädter, B, **Platis, A**, **Wehner, B**, **Scholtz, A**, **Wildmann, N**, **Hermann, M**, **Käthner, R**, **Baars, H**, **Bange, J**, **Lampert, A.** 2015. ALADINA—An unmanned research aircraft for observing vertical and horizontal distributions of ultrafine particles within the atmospheric boundary layer. *Atmospheric Measurement Techniques* **8**(4): 1627–1639. DOI: http://dx.doi.org/10.5194/amt-8-1627-2015; https://amt.copernicus.org/articles/8/1627/2015/.

Andersen, T, **Scheeren, B**, **Peters, W**, **Chen, H.** 2018. A UAV-based active AirCore system for measurements of greenhouse gases. *Atmospheric Measurement Techniques* **11**(5): 2683–2699. DOI: http://dx.doi.org/10.5194/amt-11-2683-2018; https://amt.copernicus.org/articles/11/2683/2018/.

Axford, DN. 1968. On the accuracy of wind measurements using an inertial platform in an aircraft, and an example of a measurement of the vertical mesostructure of the atmosphere. *Journal of Applied Meteorology and Climatology* **7**(4): 645–666. DOI: http://dx.doi.org/10.1175/1520-0450(1968)007<0645:OTAOWM>2.0.CO;2.

Bange, J, **Beyrich, F**, **Engelbart, DAM.** 2002. Airborne measurements of turbulent fluxes during LITFASS-98: Comparison with ground measurements and remote sensing in a case study. *Theoretical and Applied Climatology* **73**(1–2): 35–51. DOI: http://dx.doi.org/10.1007/s00704-002-0692-6.

Bange, J, **Roth, R.** 1999. Helicopter-borne flux measurements in the nocturnal boundary layer over land—A case study. *Boundary-Layer Meteorology* **92**: 295–325. DOI: http://dx.doi.org/10.1023/A:1002078712313.

Bärfuss, K, **Pätzold, F**, **Altstädter, B**, **Kathe, E**, **Nowak, S**, **Bretschneider, L**, **Bestmann, U**, **Lampert, A.** 2018. New setup of the UAS ALADINA for measuring boundary layer properties, atmospheric particles and solar radiation. *Atmosphere* **9**(1): 28. DOI: http://dx.doi.org/10.3390/atmos9010028.

Bauknecht, A, **Merz, C**, **Raffel, M.** 2017. Airborne visualization of helicopter blade tip vortices. *Journal of Visualization* **20**: 130–150. DOI: http://dx.doi.org/10.1007/s12650-016-0389-z.

Bretschneider, L, **Schlerf, A**, **Baum, A**, **Bohlius, H**, **Buchholz, M**, **Düsing, S**, **Ebert, V**, **Erraji, H**, **Frost, P**, **Käthner, R**, **Krüger, T**, **Lange, AC**, **Langner, M**, **Nowak, A**, **Pätzold, F**, **Rüdiger, J**, **Saturno, J**, **Scholz, H**, **Schuldt, T**, **Seldschopf, R**, **Sobotta, A**, **Tillmann, R**, **Wehner, B**, **Wesolek, C**, **Wolf, K**, **Lampert, A.** 2022. MesSBAR—Multicopter and instrumentation for air quality research. *Atmosphere* **13**(4). DOI: http://dx.doi.org/10.3390/atmos13040629; https://www.mdpi.com/2073-4433/13/4/629.

Buck, AL. 1976. The variable-path Lyman-alpha hygrometer and its operating characteristics. *Bulletin of the American Meteorological Society* **57**(9): 1113–1118. DOI: http://dx.doi.org/10.1175/1520-0477(1976)057<1113:TVPLAH>2.0.CO;2.

Creamean, JM, Barry, K, Hill, TCJ, Hume, C, DeMott, PJ, Shupe, MD, Dahlke, S, Willmes, S, Schmale, J, Beck, I, Hoppe, CJM, Fong, A, Chamberlain, E, Bowman, J, Scharien, R, Persson, O. 2022. Annual cycle observations of aerosols capable of ice formation in central Arctic clouds. *Nature Communications* **13**(1): 6010. DOI: http://dx.doi.org/10.1038/s41467-022-31182-x.

Drüe, C, Heinemann, G. 2007. Characteristics of intermittent turbulence in the upper stable boundary layer over Greenland. *Boundary-Layer Meteorology* **124**(3): 361–381. DOI: http://dx.doi.org/10.1007/s10546-007-9175-8.

Emeis, S, Siedersleben, S, Lampert, A, Platis, A, Bange, J, Djath, B, Stellenfleth, JS, Neumann, T. 2016. Exploring the wakes of large offshore wind farms. *Journal of Physics: Conference Series* **753**: 092014. DOI: http://dx.doi.org/10.1088/1742-6596/753/9/092014.

Fahrbach, E. 1995. The expedition ARKTIS-X/1 of the research vessel *Polarstern* in 1994. Reports on Polar Research, No. 181. Bremerhaven, Germany: Alfred Wegener Institute for Polar and Marine Research: 1–88. DOI: http://dx.doi.org/10.2312/BzP_0181_1995.

Fiehn, A, Kostinek, J, Eckl, M, Klausner, T, Gałkowski, M, Chen, J, Gerbig, C, Röckmann, T, Maazallahi, H, Schmidt, M, Korbeń, P, Neçki, J, Jagoda, P, Wildmann, N, Mallaun, C, Bun, R, Nickl, AL, Jöckel, P, Fix, A, Roiger, A. 2020. Estimating CH_4, CO_2 and CO emissions from coal mining and industrial activities in the Upper Silesian Coal Basin using an aircraft-based mass balance approach. *Atmospheric Chemistry Physics*: 12675–12695. DOI: http://dx.doi.org/10.5194/acp-20-12675-2020.

Förster, E, Huntrieser, H, Lichtenstern, M, Pätzold, F, Bretschneider, L, Lampert, A, Necki, J, Jagoda, P, Roiger, A. n.d. Quantifying methane emissions from industrial activities: A novel helicopter-borne application. *Atmospheric Measurement Techniques.*

Klausner, T, Mertens, M, Huntrieser, H, Galkowski, M, Kuhlmann, G, Baumann, R, Fiehn, A, Jöckel, P, Pühl, M, Roiger, A. 2020. Urban greenhouse gas emissions from the Berlin area: A case study using airborne CO_2 and CH_4 in situ observations in summer 2018. *Elementa: Science of the Anthropocene* **8**. DOI: http://dx.doi.org/10.1525/elementa.411.

Knust, R. 2017. Polar research and supply vessel POLARSTERN operated by the Alfred-Wegener-Institute. *Journal of Large-Scale Research Facilities JLSRF* **3**. DOI: http://dx.doi.org/10.17815/jlsrf-3-163.

Konow, H, Jacob, M, Ament, F, Crewell, S, Ewald, F, Hagen, M, Hirsch, L, Jansen, F, Mech, M, Stevens, B. 2019. A unified data set of airborne cloud remote sensing using the HALO Microwave Package (HAMP). *Earth System Science Data* **11**: 921–934. DOI: http://dx.doi.org/10.5194/essd-11-921-2019.

Kostinek, J, Roiger, A, Eckl, M, Fiehn, A, Luther, A, Wildmann, N, Klausner, T, Fix, A, Knote, C, Stohl, A, Butz, A. 2021. Estimating upper Silesian coal mine methane emissions from airborne in situ observations and dispersion modeling. *Atmospheric Chemistry Physics* **21**(11): 8791–8807. DOI: http://dx.doi.org/10.5194/acp-21-8791-2021.

Krause, G. 1996. The expedition ARKTIS-XI/2 of RV *Polarstern* in 1995. Reports on Polar Research, No. 197. Bremerhaven, Germany: Alfred Wegener Institute: 1–70.

Kumala, W, Haman, K, Kopec, M, Khelif, D, Malinowski, S. 2013. Modified ultrafast thermometer UFT-M and temperature measurements during Physics of Stratocumulus Top (POST). *Atmospheric Measurement Techniques* **6**: 2043–2054. DOI: http://dx.doi.org/10.5194/amt-6-2043-2013.

Lampert, A, Altstädter, B, Bärfuss, K, Bretschneider, L, Sandgaard, J, Michaelis, J, Lobitz, L, Asmussen, M, Damm, E, Käthner, R, Krüger, T, Lüpkes, C, Nowak, S, Peuker, A, Rausch, T, Reiser, F, Scholtz, A, Sotomayor Zakharov, D, Gaus, D, Bansmer, S, Wehner, B, Pätzold, F. 2020a. Unmanned aerial systems for investigating the polar atmospheric boundary layer—Technical challenges and examples of applications. *Atmosphere* **11**(4): 416. DOI: http://dx.doi.org/10.3390/atmos11040416.

Lampert, A, Bärfuss, K, Platis, A, Siedersleben, S, Djath, B, Cañadillas, B, Hunger, R, Hankers, R, Bitter, M, Feuerle, T, Schulz, H, Rausch, T, Angermann, M, Schwithal, A, Bange, J, Schulz-Stellenfleth, J, Neumann, T, Emeis, S. 2020b. In situ airborne measurements of atmospheric and sea surface parameters related to offshore wind parks in the German Bight. *Earth System Science Data* **12**(2): 935–946. DOI: http://dx.doi.org/10.5194/essd-12-935-2020.

Lampert, A, Hartmann, J, Pätzold, F, Lobitz, L, Hecker, P, Kohnert, K, Larmanou, E, Serafimovich, A, Sachs, T. 2018. Comparison of Lyman-alpha and LI-COR infrared hygrometers for airborne measurement of turbulent fluctuations of water vapour. *Atmospheric Measurement Techniques* **11**(4): 2523–2536. DOI: http://dx.doi.org/10.5194/amt-11-2523-2018.

Lampert, A, Pätzold, F, Asmussen, MO, Lobitz, L, Krüger, T, Rausch, T, Sachs, T, Wille, C, Sotomayor Zakharov, D, Gaus, D, Bansmer, S, Damm, E. 2020c. Studying boundary layer methane isotopy and vertical mixing processes at a rewetted peatland site using an unmanned aircraft system. *Atmospheric Measurement Techniques* **13**(4): 1937–1952. DOI: http://dx.doi.org/10.5194/amt-13-1937-2020; https://amt.copernicus.org/articles/13/1937/2020/.

Lampert, A, Pätzold, F, Jiménez, MA, Lobitz, L, Martin, S, Lohmann, G, Canut, G, Legain, D, Bange, J, Martínez-Villagrasa, D, Cuxart, J. 2016. A study of local turbulence and anisotropy during the

afternoon and evening transition with an unmanned aerial system and mesoscale simulation. *Atmospheric Chemistry and Physics* **16**(12): 8009–8021. DOI: http://dx.doi.org/10.5194/acp-16-8009-2016.

Leishman, J. 2000. *Principles of helicopter aerodynamics.* Cambridge, UK: Cambridge University Press: 63–66.

Lonardi, M, Pilz, C, Akansu, EF, Dahlke, S, Egerer, U, Ehrlich, A, Griesche, H, Heymsfield, AJ, Kirbus, B, Schmitt, CG, Shupe, MD, Siebert, H, Wehner, B, Wendisch, M. 2022. Tethered balloon-borne profile measurements of atmospheric properties in the cloudy atmospheric boundary layer over the Arctic sea ice during MOSAiC: Overview and first results. *Elementa: Science of the Anthropocene* **10**(1). DOI: http://dx.doi.org/10.1525/elementa.2021.000120.

Martin, S, Bange, J, Beyrich, F. 2011. Meteorological profiling of the lower troposphere using the research UAV "M2AV Carolo." *Atmospheric Measurement Techniques* **4**(4): 705–716. DOI: http://dx.doi.org/10.5194/amt-4-705-2011.

Muschinski, A, Wode, C. 1998. First in situ evidence for coexisting submeter temperature and humidity sheets in the lower free troposphere. *Journal of the Atmospheric Sciences* **55**(18): 2893–2906. DOI: http://dx.doi.org/10.1175/1520-0469(1998)055<2893.FISEFC>2.0.CO;2.

Nicolaus, M, Perovich, DK, Spreen, G, Granskog, MA, von Albedyll, L, Angelopoulos, M, Anhaus, P, Arndt, S, Belter, HJ, Bessonov, V, Birnbaum, G, Brauchle, J, Calmer, R, Cardellach, E, Cheng, B, Clemens-Sewall, D, Dadic, R, Damm, E, de Boer, G, Demir, O, Dethloff, K, Divine, DV, Fong, AA, Fons, S, Frey, MM, Fuchs, N, Gabarró, C, Gerland, S, Goessling, HF, Gradinger, R, Haapala, J, Haas, C, Hamilton, J, Hannula, HR, Hendricks, S, Herber, A, Heuzé, C, Hoppmann, M, Høyland, KV, Huntemann, M, Hutchings, JK, Hwang, B, Itkin, P, Jacobi, HW, Jaggi, M, Jutila, A, Kaleschke, L, Katlein, C, Kolabutin, N, Krampe, D, Kristensen, SS, Krumpen, T, Kurtz, N, Lampert, A, Lange, BA, Lei, R, Light, B, Linhardt, F, Liston, GE, Loose, B, Macfarlane, AR, Mahmud, M, Matero, IO, Maus, S, Morgenstern, A, Naderpour, R, Nandan, V, Niubom, A, Oggier, M, Oppelt, N, Pätzold, F, Perron, C, Petrovsky, T, Pirazzini, R, Polashenski, C, Rabe, B, Raphael, IA, Regnery, J, Rex, M, Ricker, R, Riemann-Campe, K, Rinke, A, Rohde, J, Salganik, E, Scharien, RK, Schiller, M, Schneebeli, M, Semmling, M, Shimanchuk, E, Shupe, MD, Smith, MM, Smolyanitsky, V, Sokolov, V, Stanton, T, Stroeve, J, Thielke, L, Timofeeva, A, Tonboe, RT, Tavri, A, Tsamados, M, Wagner, DN, Watkins, D, Webster, M, Wendisch, M. 2022. Overview of the MOSAiC expedition: Snow and sea ice. *Elementa: Science of the Anthropocene* **10**(1). DOI: http://dx.doi.org/10.1525/elementa.2021.000046.

Nixdorf, U, Dethloff, K, Rex, MMS, Sommerfeld, A, Perovich, DK, Nicolaus, M, Heuzé, C, Rabe, B, Loose, B, Damm, E, Gradinger, R, Fong, A,

Maslowski, W, Rinke, A, Kwok, R, Spreen, G, Wendisch, M, Herber, A, Hirsekorn, M, Mohaupt, V, Frickenhaus, S, Immerz, A, Weiss-Tuider, K, König, B, Mengedoht, D, Regnery, J, Gerchow, P, Ransby, D, Krumpen, T, Morgenstern, A, Haas, C, Kanzow, T, Rack, FR, Saitzev, V, Sokolov, V, Makarov, A, Schwarze, S, Wunderlich, T, Wurr, K, Boetius, A. 2021. MOSAiC extended acknowledgement. Zenodo. DOI: http://dx.doi.org/10.5281/zenodo.5541624.

Platis, A, Altstädter, B, Wehner, B, Wildmann, N, Lampert, A, Hermann, M, Birmili, W, Bange, J. 2016. An observational case study on the influence of atmospheric boundary-layer dynamics on new particle formation. *Boundary-Layer Meteorology* **158**: 67–92. DOI: http://dx.doi.org/10.1007/s10546-015-0084-y.

Rabe, B, Heuzé, C, Regnery, J, Aksenov, Y, Allerholt, J, Athanase, M, Bai, Y, Basque, C, Bauch, D, Baumann, TM, Chen, D, Cole, ST, Craw, L, Davies, A, Damm, E, Dethloff, K, Divine, DV, Doglioni, F, Ebert, F, Fang, YC, Fer, I, Fong, AA, Gradinger, R, Granskog, MA, Graupner, R, Haas, C, He, H, He, Y, Hoppmann, M, Janout, M, Kadko, D, Kanzow, T, Karam, S, Kawaguchi, Y, Koenig, Z, Kong, B, Krishfield, RA, Krumpen, T, Kuhlmey, D, Kuznetsov, I, Lan, M, Laukert, G, Lei, R, Li, T, Torres-Valdés, S, Lin, L, Lin, L, Liu, H, Liu, N, Loose, B, Ma, X, McKay, R, Mallet, M, Mallett, RDC, Maslowski, W, Mertens, C, Mohrholz, V, Muilwijk, M, Nicolaus, M, O'Brien, JK, Perovich, D, Ren, J, Rex, M, Ribeiro, N, Rinke, A, Schaffer, J, Schuffenhauer, I, Schulz, K, Shupe, MD, Shaw, W, Sokolov, V, Sommerfeld, A, Spreen, G, Stanton, T, Stephens, M, Su, J, Sukhikh, N, Sundfjord, A, Thomisch, K, Tippenhauer, S, Toole, JM, Vredenborg, M, Walter, M, Wang, H, Wang, L, Wang, Y, Wendisch, M, Zhao, J, Zhou, M, Zhu, J. 2022. Overview of the MOSAiC expedition: Physical oceanography. *Elementa: Science of the Anthropocene* **10**(1). DOI: http://dx.doi.org/10.1525/elementa.2021.00062.

Schauer, U, Kattner, G. 2004. The expedition ARKTIS XIX/1 a, b and XIX/2 of the Research Vessel *Polarstern* in 2003. Reports on Polar Research, No. 481. Bremerhaven, Germany: Alfred Wegener Institute: 1–198. DOI: http://dx.doi.org/10.2312/BzPM_0481_2004.

Schuldt, T, Gkatzelis, G, Wesolek, C, Rohrer, F, Winter, B, Kuhlbusch, T, Kiendler-Scharr, A, Tillmann, R. 2023. Electrochemical sensors on board a Zeppelin NT: In-flight evaluation of low-cost trace gas measurements. *Atmospheric Measurement Techniques* **16**: 373–386. DOI: http://dx.doi.org/10.5194/amt-16-373-2023.

Shupe, MD, Rex, M, Blomquist, B, Persson, POG, Schmale, J, Uttal, T, Althausen, D, Angot, H, Archer, S, Bariteau, L, Beck, I, Bilberry, J, Bucci, S, Buck, C, Boyer, M, Brasseur, Z, Brooks, IM, Calmer, R, Cassano, J, Castro, V, Chu, D, Costa,

D, Cox, CJ, Creamean, J, Crewell, S, Dahlke, S, Damm, E, de Boer, G, Deckelmann, H, Dethloff, K, Dütsch, M, Ebell, K, Ehrlich, A, Ellis, J, Engelmann, R, Fong, AA, Frey, MM, Gallagher, MR, Ganzeveld, L, Gradinger, R, Graeser, J, Greenamyer, V, Griesche, H, Griffiths, S, Hamilton, J, Heinemann, G, Helmig, D, Herber, A, Heuzé, C, Hofer, J, Houchens, T, Howard, D, Inoue, J, Jacobi, HW, Jaiser, R, Jokinen, T, Jourdan, O, Jozef, G, King, W, Kirchgaessner, A, Klingebiel, M, Krassovski, M, Krumpen, T, Lampert, A, Landing, W, Laurila, T, Lawrence, D, Lonardi, M, Loose, B, Lüpkes, C, Maahn, M, Macke, A, Maslowski, W, Marsay, C, Maturilli, M, Mech, M, Morris, S, Moser, M, Nicolaus, M, Ortega, P, Osborn, J, Pätzold, F, Perovich, DK, Petäjä, T, Pilz, C, Pirazzini, R, Posman, K, Powers, H, Pratt, KA, Preußer, A, Quéléver, L, Radenz, M, Rabe, B, Rinke, A, Sachs, T, Schulz, A, Siebert, H, Silva, T, Solomon, A, Sommerfeld, A, Spreen, G, Stephens, M, Stohl, A, Svensson, G, Uin, J, Viegas, J, Voigt, C, von der Gathen, P, Wehner, B, Welker, JM, Wendisch, M, Werner, M, Xie, Z, Yue, F. 2022. Overview of the MOSAiC expedition: Atmosphere. *Elementa: Science of the Anthropocene* **10**(1). DOI: http://dx.doi.org/10.1525/elementa.2021.00060.

Siebert, H, Beals, M, Bethke, J, Bierwirth, E, Conrath, T, Dieckmann, K, Ditas, F, Ehrlich, A, Farrell, D, Hartmann, S, Izaguirre, MA, Katzwinkel, J, Nuijens, L, Roberts, G, Schäfer, M, Shaw, RA, Schmeissner, T, Serikov, I, Stevens, B, Stratmann, F, Wehner, B, Wendisch, M, Werner, F, Wex, H. 2013. The finescale structure of the trade wind cumuli over Barbados—An introduction to the CARRIBA project. *Atmospheric Chemistry and Physics* **13**(19): 10061–10077. DOI: http://dx.doi.org/10.5194/acp-13-10061-2013.

Siebert, H, Franke, H, Lehmann, K, Maser, R, Saw, EW, Schell, D, Shaw, RA, Wendisch, M. 2006. Probing finescale dynamics and microphysics of clouds with helicopter-borne measurements. *Bulletin of the American Meteorological Society* **87**(12): 1727–1738. DOI: http://dx.doi.org/10.1175/BAMS-87-12-1727.

Siebert, H, Szodry, KE, Egerer, U, Wehner, B, Henning, S, Chevalier, K, Lückerath, J, Welz, O, Weinhold, K, Lauermann, F, Gottschalk, M, Ehrlich, A,

Wendisch, M, Fialho, P, Roberts, G, Allwayin, N, Schum, S, Shaw, RA, Mazzoleni, C, Mazzoleni, L, Nowak, JL, Malinowski, SP, Karpinska, K, Kumala, W, Czyzewska, D, Luke, EP, Kollias, P, Wood, R, Mellado, JP. 2021. Observations of aerosol, cloud, turbulence, and radiation properties at the top of the marine boundary layer over the Eastern North Atlantic Ocean: The ACORES campaign. *Bulletin of the American Meteorological Society* **102**(1): E123–E147. DOI: http://dx.doi.org/10.1175/BAMS-D-19-0191.1; https://journals.ametsoc.org/view/journals/bams/102/1/BAMS-D-19-0191.1.xml.

Sperzel, T, Jäkel, E, Pätzold, F, Lampert, A, Niehaus, H, Spreen, G, Rosenburg, S, Birnbaum, G, Neckel, N, Wendisch, M. 2023. Broadband albedo measurements and surface type classification from HELiPOD and helicopter during MOSAiC. *Scientific Data* **10**: 584. DOI: https://doi.org/10.1038/s41597-023-02492-6.

van den Kroonenberg, A, Bange, J. 2007. Turbulent flux calculation in the polar stable boundary layer: Multiresolution flux decomposition and wavelet analysis. *Journal of Geophysical Research* **112**(D06112). DOI: http://dx.doi.org/10.1029/2006JD007819.

Vinković, K, Andersen, T, de Vries, M, Kers, B, van Heuven, S, Peters, W, Hensen, A, van den Bulk, P, Chen, H. 2022. Evaluating the use of an unmanned aerial vehicle (UAV)-based active AirCore system to quantify methane emissions from dairy cows. *Science of The Total Environment* **831**: 154898. DOI: http://dx.doi.org/10.1016/j.scitotenv.2022.154898; https://www.sciencedirect.com/science/article/pii/S004896972201991X.

Wehner, B, Philippin, S, Wiedensohler, A. 2002. Design and calibration of a thermodenuder with and improved heating unit to measure the size-dependent volatile fraction of aerosol particles. *Journal of Aerosol Science* **33**(7): 1087–1093. DOI: http://dx.doi.org/10.1016/S0021-8502(02)00056-3.

Wehner, B, Werner, F, Ditas, F, Shaw, RA, Kulmala, M, Siebert, H. 2015. Observations of new particle formation in enhanced UV irradiance zones near cumulus clouds. *Atmospheric Chemistry and Physics* **15**: 11701–11711. DOI: http://dx.doi.org/10.5194/acp-15-11701-2015.